Novel insights into deep groundwater exploration by geophysical estimation of

hard rock permeability

Muhammad Hasan [1, 2, 3,*], **Lijun Su** [1, 2, 3, **]

[1] *State Key Laboratory of Mountain Hazards and Engineering Resilience, Institute of Mountain*

Hazards and Environment, Chinese Academy of Sciences, Chengdu 610299, China

[2] *China-Pakistan Joint Research Center on Earth Sciences, CAS-HEC, Islamabad, Pakistan*

[3] *University of Chinese Academy of Sciences, Beijing 100049, China*

*Corresponding authors:

Muhammad Hasan: Email: mhasan@imde.ac.cn; ORCID: https://orcid.org/0000-0001-6804-7962; Phone Number: +86-13051361710

Lijun Su: Email: sulijun1976@163.com; ORCID: https://orcid.org/0000-0001-9972-4698

Corresponding authors' postal address: State Key Laboratory of Mountain Hazards and Engineering Resilience, Institute of Mountain Hazards and Environment, Chinese Academy of Sciences, Chengdu 610299, China

Abstract

Deep groundwater exploration in hard rock terrains is critical in regions where deep aquifers may offer long-term water security amidst an increasing scarcity. However, such exploration is globally challenged by geological complexity and the limitations of traditional investigative techniques. Accurate estimation of hydraulic parameters, particularly permeability (k), is essential for effective groundwater management and future resource planning. Conventional borehole-based methods for measuring k are invasive, costly, time-consuming, and limited to sparse, point-scale observations, making them inadequate for characterizing deep and heterogeneous aquifer systems. Geophysical methods offer a promising non-invasive alternative, enabling broader spatial coverage with reduced surface disturbance. Previous empirical geophysical approaches, such as vertical electrical sounding (VES), are generally restricted to shallow depths (<200 m), relatively homogeneous geological settings, and one-dimensional interpretations. This study demonstrates, for the first time, the use of controlled-source audio-frequency magnetotellurics (CSAMT) to estimate two- and three-dimensional k distributions to depths exceeding 1 km in crystalline and sedimentary terrains. The method relies on an empirical resistivity–permeability relationship calibrated using 116 core samples from six boreholes (0–200 m). While the specific equation derived in this study is site-specific to the Jinji area and should not be directly transferred elsewhere, the broader methodology, integrating CSAMT resistivity with local borehole calibration, offers a transferable framework for k estimation in other complex geological settings. The results show that CSAMT, when calibrated with borehole data, can reliably capture deep subsurface variability and produce spatially continuous hydrogeological models in hard rock terrains. While CSAMT inversion is inherently ill-posed, the incorporation of ground-truth data significantly enhances model robustness and

2

46 interpretability. By reducing dependence on extensive drilling, this approach represents a

47 significant advancement in deep groundwater exploration. It provides a scalable methodology for

48 sustainable groundwater resource management, while emphasizing the need for local calibration

49 in any new application.

50 **Keywords:** Permeability; Geophysical methods; Hydraulic parameters; Groundwater; Hard rock;

51 Hydrogeological models

52 **1 Introduction**

53 Metamorphic and igneous rocks dominate Earth's crust and cover about one-third of its surface

54 (Amiotte Suchet et al., 2003). In hard rock terrains, groundwater research focuses on delineating

55 subsurface structures, such as faults and fractures that control water storage and flow (Fernando

56 and Pacheco, 2015; Hasan et al., 2021). A key parameter in this context is aquifer potential,

57 which reflects the capacity of rock formations to store and transmit groundwater and is

58 influenced by lithology, structural complexity, mineral composition, weathering, and infiltration

59 depth (Majumdar and Das, 2011; Zhu et al., 2017). However, accurately characterizing the

60 lateral and vertical heterogeneity of these properties remains challenging due to limited data and

61 the complexity of massive rock units (Dewandel et al., 2006). In such settings, conventional

62 methods often fall short, leading to inefficient or unsustainable groundwater development

63 (Nwosu et al., 2013; Worthington et al., 2016). Developing cost-effective and reliable

64 approaches for subsurface assessment is therefore essential for managing groundwater in hard

65 rock environments.

66 Groundwater at depths beyond 500 m is typically isolated from surface hydrological

67 influences and often exhibits brackish or saline characteristics (Ferguson et al., 2023). Its

68 strategic importance is increasingly recognized, particularly in geologically- and

69 environmentally-constrained settings (Gleeson et al., 2014). In the Jinji region, several factors

70 necessitate focused investigation of deep aquifers. Surface water is scarce and unreliable, while

71 the shallow subsurface is dominated by fresh granite, which has inherently low porosity and

72 permeability, limiting groundwater availability. By contrast, deeper fractured zones in granite,

73 sandstone, and hornstone present more favorable hydrogeological conditions. Recent national

74 water initiatives in China have emphasized deep subsurface exploration in structurally complex

75 terrains to identify underutilized aquifers for enhancing long-term water security.

76 Comprehensive assessment of these deep reserves is essential to evaluate their recharge potential

77 and integrate them into sustainable resource management strategies (Condon et al., 2020; Hasan

78 and Shang, 2022). As pressure on surface and shallow groundwater intensifies, deep aquifers

79 may serve as a vital buffer against increasing environmental and socio-economic stress.

80 Multiple studies have documented the rapid depletion of global groundwater reserves,

81 raising serious concerns about long-term water sustainability (Wada et al., 2010; Laghari et al.,

82 2012; Jasechko et al., 2024). Addressing this challenge requires accurate and detailed

83 assessments of groundwater resources, which depend critically on a clear understanding of

84 subsurface hydraulic properties. Permeability (k) is a key parameter that describes the ease with

85 which fluids can move through a porous medium, while the capacity to store water is more

86 directly characterized by porosity. This parameter is crucial for aquifer analysis in various

87 hydrogeological settings (Allègre et al., 2016; Esmaeilpour et al., 2023; Carbillet et al., 2024).

88 Borehole testing remains the standard method for estimating k and related aquifer parameters

89 (De Lima and Niwas, 2000; Hasan et al., 2021). However, borehole investigations are often

90 limited by high costs, logistical challenges, and poor spatial coverage, particularly in rugged

4

terrains, while offering only localized information with limited ability to image lateral and deep structures (Singh, 2005; Fiandaca et al., 2018). These limitations contribute to uncertainties in groundwater assessments, especially in data-scarce regions (Hasan and Shang, 2022). Alternatively, it is essential to develop methods that minimize reliance on costly drilling while still enabling reliable estimation of permeability within prospective rock formations.

Geophysical methods are widely and effectively employed to enhance subsurface characterization in groundwater studies (Daily et al., 1992; Jardani et al., 2007; Hinnell et al., 2010; Fu et al., 2013; Jiang et al., 2014; Kouadio et al., 2023). Compared to conventional drilling, these techniques offer significant advantages in cost, deployment speed, environmental impact, and spatial extent (Hu et al., 2013; Fusheng et al., 2022). Their ability to image subsurface variations in both vertical and lateral dimensions makes them particularly effective in heterogeneous terrains (Hasan et al., 2025). Among them, resistivity-based methods are widely used due to their sensitivity to lithology, porosity, fractures, and fluid content (Hasan et al., 2021; Asfahani, 2023). Common techniques include electrical resistivity tomography (ERT), vertical electrical sounding (VES), and electromagnetic methods such as magnetotellurics (MT), time-domain electromagnetics (TDEM), and controlled-source audio-frequency magnetotellurics (CSAMT) (Soupios et al., 2007; Bauer-Gottwein et al., 2010; Pollock and Cirpka, 2012; Jiang et al., 2014; Di et al., 2020). A comparative summary of these methods (Table 1) highlights their relative strengths and limitations in terms of ~~depth~~ penetration depth, spatial resolution, sensitivity to cultural noise, and cost. VES is cost-effective but limited to shallow one-dimensional profiling (<200 m) (Niwas and De Lima, 2003; Majumdar and Das, 2011). ERT improves resolution and enables 2D/3D imaging up to ~300 m but requires intensive fieldwork and is less effective in extreme resistivity environments (Abbas et al., 2022; Hasan and Shang,

5

114   2022). For deeper targets, electromagnetic methods such as TDEM, MT, and CSAMT are often

115   employed (Bauer-Gottwein et al., 2010; Di et al., 2020; Gonzalez-Duque et al., 2024). MT

116   achieves the greatest ~~depth~~ penetration depth (up to tens of kilometers) but often sacrifices

117   resolution in the upper crust and is highly susceptible to cultural noise (Simpson and Bahr,

118   2005). TDEM provides rapid deployment and intermediate depth coverage (hundreds of meters)

119   but suffers reduced sensitivity in resistive hard rock (Bauer-Gottwein et al., 2010). By contrast,

120   CSAMT bridges these approaches: with a controlled source and frequency tuning, it achieves

121   intermediate-to-deep penetration (>1000 m) with improved resolution in resistive hard rock

122   settings and strong immunity to cultural noise (Smith and Booker, 1991; Zonge and Hughes,

123   1991; Wang et al., 2015; Zhang et al., 2021). The choice between resistivity and electromagnetic

124   techniques is contingent upon parameters like investigation depth, resolution requirements,

125   geological complexity, and logistical constraints (Majumdar and Das, 2011; Hasan et al., 2025).

126   Given the objectives of this study, to characterize deep fractured aquifers in crystalline and

127   sedimentary rocks under complex geological conditions, CSAMT was selected as the most

128   suitable technique. Its combination of ~~depth~~ penetration depth, resolution, and robustness against

129   noise provides a practical balance between regional coverage and site-specific imaging, enabling

130   the development of 2D and 3D permeability models that are otherwise difficult to achieve with

131   alternative methods.

132   In fractured rocks like granite, metamorphic, and sandstone formations, fluid flow is

133   largely controlled by fracture networks rather than matrix porosity. Accurate hydraulic

134   assessment in such settings benefits from integrated geophysical and hydrogeological approaches

135   to better capture spatial variability and improve flow modeling (Hasan et al., 2021; Abbas et al.,

136   2022). Resistivity-based techniques are particularly valuable for delineating subsurface structures

6

and identifying water-bearing zones. Because electrical resistivity is sensitive to porosity, saturation, fracture density, and fluid salinity, it is increasingly used to infer k in heterogeneous geological settings (Mudunuru et al., 2022; Yan et al., 2024). Permeability is influenced by numerous parameters, including porosity, fracture density and orientation, grain size distribution, degree of weathering, pore connectivity, and saturation level, highlighting the utility of resistivity measurements as indicators for evaluating groundwater flow potential (Gerke et al., 2011; Worthington et al., 2016; Pellet et al., 2024).

Empirical and semi-empirical models have been developed to estimate hydraulic properties from geophysical measurements, particularly in data-sparse regions (Niwas and De Lima, 2003; Singh, 2005; Soupios et al., 2007; Hasan et al., 2021; Asfahani, 2023). In parallel, resistivity-based methods and hydrogeophysical inversion techniques have been developed to more rigorously estimate hydraulic parameters by integrating petrophysical relationships within geophysical modeling frameworks (Daily et al., 1992; Ferré et al., 2009; Binley et al., 2010; Hinnell et al., 2010; Herckenrath et al., 2012; Pollock and Cirpka, 2012; Herckenrath et al., 2013; Binley et al., 2015). These approaches have improved resolution in parameter estimation, particularly in shallow, unconsolidated, or relatively homogeneous settings. However, applications to deep, fractured, and lithologically complex environments remain limited, especially in terms of producing volumetric k models at kilometer-scale depths. Despite these advances, generation of detailed 2D and 3D k maps from resistivity data in deep, hard-rock terrains is constrained by limited borehole control, significant geological heterogeneity, and the ill-posed nature of geophysical inversion. In such contexts, integrating resistivity data with borehole measurements presents a practical, cost-effective solution for characterizing aquifer properties over large areas and depth ranges. This study builds on prior hydrogeophysical

research by introducing a novel application of the CSAMT method for volumetric k modeling in a complex, fractured hard-rock setting. While previous studies have applied resistivity-based techniques to estimate hydraulic properties, this is the first to utilize CSAMT for constructing the detailed 2D and 3D k modeling beyond 1000 m depth in geologically heterogeneous terrains comprising hornstone, granite, and sandstone. Few available drilling tests were used to calibrate CSAMT-derived resistivity with laboratory-measured k, allowing the resulting empirical relationship to be applied across the broader survey domain. Several CSAMT profiles were conducted along and beyond the borehole locations, and the calibrated resistivity–permeability correlation was used to generate spatially continuous subsurface models in regions lacking direct borehole data. This integration resulted in a robust, data-constrained workflow capable of revealing k variations across diverse rock units and lithological boundaries. The method offers a practical and scalable alternative to extensive drilling campaigns, enabling a more detailed and cost-efficient evaluation of deep groundwater potential in structurally complex terrains.

Ultimately, this work extends the scope of hydrogeophysical methods by demonstrating the feasibility of applying CSAMT for deep hydraulic parameter estimation in hard rock. It bridges a critical methodological gap in hard-rock hydrogeology and sets the foundation for future CSAMT-based volumetric modeling in similarly challenging environments. This study aims to develop and apply a geophysical-based approach for mapping the spatial distribution of k in deep, hard-rock settings. By integrating CSAMT data with targeted borehole measurements, this research enhances 2D and 3D hydrogeological assessments across heterogeneous lithologies in structurally complex terrains. It also minimizes reliance on extensive drilling, demonstrating the value of non-invasive geophysical techniques as a cost-effective alternative for deep groundwater exploration.

183 **Table 1**

184 Comparative overview of geophysical methods for hydrogeological investigations

Method	Typical depth of investigation	Spatial resolution	Cultural noise susceptibility	Cost and logistics	Suitability for deep hard rock aquifers
VES (Vertical Electrical Sounding)	<200 m	1D only, low lateral resolution	Low–Moderate	Low, rapid	Limited to shallow, homogeneous settings
ERT (Electrical Resistivity Tomography)	Up to ~300 m	High (2D/3D imaging)	Moderate	Moderate; requires dense electrode arrays	Excellent for shallow fractured/karst zones, but inadequate for >500 m depth
TDEM (Time-Domain Electromagnetics)	200–600 m (occasionally deeper)	Moderate	Moderate; affected by near-surface conductivity	Moderate, rapid deployment	Useful for intermediate depths; less effective in highly resistive hard rocks
MT (Magnetotellurics)	Hundreds of m to tens of km	Low in upper crust, improves at depth	High; strongly affected by cultural noise	High; long acquisition times	Excellent for regional mapping and geothermal studies; less suited for site-specific aquifer modeling
CSAMT (Controlled-Source Audio-MT)	~200–1,300 m (depending on frequency & geology)	Moderate–High (2D/3D capable)	Low; controlled source minimizes noise	Moderate; portable, adaptable	Well-suited for imaging deep, resistive, heterogeneous aquifers; strong balance

9

	of depth, resolution, and adaptability

185

2 Methods

187 This research integrates limited drilling information with geophysical data to estimate *k* for both

188 2D and 3D evaluations of groundwater resources over the entire investigated site (Fig. 1a). The

189 main stages of the methodology are summarized in the flowchart shown in Fig. 1b.

190 (a)　　　　　　　　　　(b)
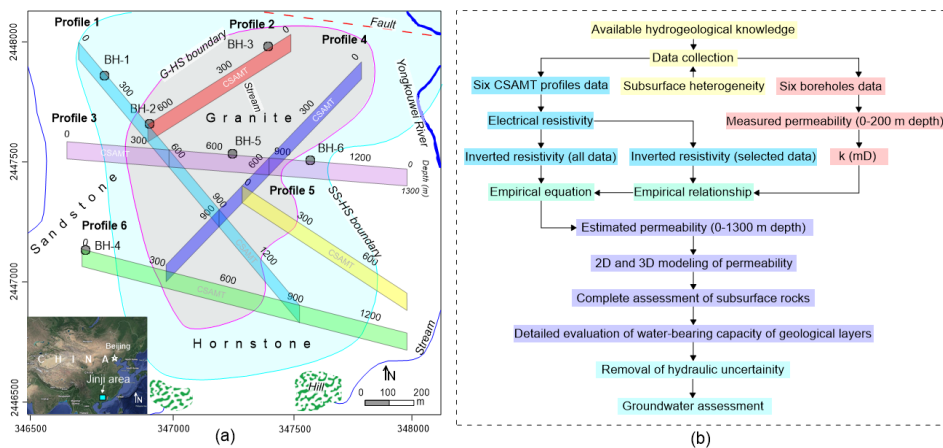
Fig. 1. (a) The site map displaying six boreholes (BH-1 to BH-6) and six CSAMT survey profiles (1–6). The map also illustrates the simplified geological and hydrogeological setting, including the dominant rock types (granite, hornstone, and sandstone), the granite–hornstone (G–HS) and sandstone–hornstone (SS–HS) boundaries, major fault lines, streams, rivers, and surrounding mountainous terrain; (b) Flowchart illustrating the methodology for generating 2D and 3D *k* models to enable comprehensive assessments of groundwater resources across extensive areas

10

2.1 Study area and hydrogeological settings

This study is part of a national initiative in South Guangdong, China, focused on deep subsurface exploration, including groundwater resource assessment and infrastructure development such as the Jiangmen Underground Neutrino Observatory (JUNO) (Hasan et al., 2025). These actions contribute to China's national agenda toward sustainable deep-earth resource utilization. This research was conducted in the Jinji region, a geologically complex area prioritized for deep groundwater exploration (Fig. 1a). The region lies within a subtropical monsoonal climate zone, receiving ~1981 mm of annual rainfall. Topography ranges from low hills to mountainous terrain (39–539.9 m elevation), with dense vegetation and varied slopes. The northern part is relatively flat, while the south includes prominent features such as the Dashishan and Qilongding Mountains. Surface drainage is primarily controlled by the Yongkouwei River in the northeast.

Geologically, the Jinji area has evolved through successive tectono-magmatic processes linked to the Yanshanian, Indosinian, and Caledonian mountain-building phases, resulting in a lithologically diverse landscape of granite, sandstone, and hornstone (Qin, 2017). Granite intrusions reflect deep crustal magmatism, while hornstone indicates contact metamorphism. Overlying Paleogene sediments record later basin development. Tectonic structuring in the area is largely influenced by the Kaiping fault-fold complex, which includes reverse, thrust, and strike-slip faults formed under prolonged crustal compression and later modified by strike-slip tectonics. These northeast-trending structures govern subsurface architecture and groundwater flow pathways (Yang et al., 2021). Fractures and joints are widespread in granite, sandstone, and hornstone, varying by lithology and tectonic history. These brittle features act as primary

11

219　conduits for groundwater, with their alignment along major faults highlighting the tight coupling

220　between structural geology and hydrogeology.

221　　　This study focuses on the vertical stratification of aquifer-bearing formations. Productive

222　groundwater is mainly stored in deep, fractured sandstone units, overlain by low-permeability

223　granite that limits vertical recharge. An intermediate hornstone layer separates the two, with

224　moderate hydraulic properties and limited connectivity. This configuration isolates the deep

225　aquifer from surface influences, rendering shallow investigations ineffective. Deep-targeted

226　exploration is thus essential for identifying and managing these concealed high-potential

227　groundwater resources in a structurally complex hard rock setting.

228　**2.2 CSAMT survey**

229　**2.2.1 Theoretical background**

230　CSAMT is extensively employed for hard rock evaluations due to its ability to resolve deep

231　subsurface features (Fu et al., 2013; Wang et al., 2015; Di et al., 2020; Kouadio et al., 2023).

232　This method employs a distant, regulated electric source that transmits signals into the ground,

233　while electric and magnetic field components are recorded at receiving stations (Zonge and

234　Hughes, 1991). CSAMT uses frequency-dependent EM wave penetration; lower frequencies

235　reach greater depths, depending on rock conductivity (Cagniard, 1953; Borah and Patro, 2019).

236　Signal frequencies are extracted using Fourier transforms from time-series field measurements

237　(Simpson and Bahr, 2005). A typical CSAMT setup uses electric dipole sources arranged

238　between 1 and 2 km intervals, with 5–10 km offsets based on the required penetration depth and

239　lithological conditions.

240   Resistivity is calculated by analyzing orthogonal electric and magnetic field magnitudes.

241 Vertical resolution typically ranges from 5%–20% of the depth of investigation (DOI), which

242 spans ~20–1000 m. Shallow depths (20–100 m) offer finer resolution, while deeper imaging is

243 coarser due to signal attenuation. DOI increases with lower frequencies and higher subsurface

244 resistivity (Borah and Patro, 2019). Lateral resolution depends on station spacing (10–200 m);

245 wider spacing enhances signal strength and coherence (Simpson and Bahr, 2005). Field setups

246 include portable receivers with electrodes and magnetic sensors to record signals, which are

247 filtered and amplified in real time. Effective survey planning is essential to mitigate interference

248 from fences, power lines, and radio transmitters. Final resistivity models are presented in plan,

249 fence, cross-sectional, or 3D formats.

250 **2.2.2 Survey design and procedures**

251 Data acquisition was performed along six CSAMT lines (1–6) using a 50 m interval between

252 stations, selected based on geological targets, terrain accessibility, structural orientation,

253 integration with borehole data, and expected resistivity contrasts. These optimized profiles

254 improved subsurface resolution and minimized interpretational ambiguity. The DOI reached

255 approximately 1300 m. Measurements were conducted in scalar Transverse Magnetic (TM)

256 mode, recording E- and H-field vectors in both longitudinal and transverse directions along the

257 survey profiles. EMAP stations were spaced ~50 m from electrodes. A 50 Hz linear filter was

258 implemented under Gain Mode X1 settings. Transmission current spanned 2.6–18 A across the

259 7680 Hz to 1 Hz range.

260   Data acquisition utilized a Phoenix Geophysics V8 multifunction receiver and TXU-30

261 transmitter, capable of 30 kW output, transmitting up to 1000 V and 40 A. The system operated

262 across 34 frequencies (1–7680 Hz), with transmitter–receiver distances of 9.3–12.5 km. Non-

263   polarized electrodes captured electric fields, while magnetic fields were recorded using AMTC-

264   30 sensors (0.1–10,000 Hz). Each site recorded two orthogonal electric and three orthogonal

265   magnetic components, enabling full impedance tensor calculation. Survey positions were

266   determined using Hi-Target V30 RTK and Trimble XH GPS, ensuring sub-meter accuracy.

267   Coordinates were computed and transmitted to the navigation system for real-time positioning.

268   Survey point spacing remained consistent, with system quality metrics indicating 3–5%

269   variability. Design tolerances were met: RMS error $< \pm 5\%$, inter-point error $< 10\%$, horizontal

270   and vertical tolerances of 2.33 mm and 1.67 mm, respectively. Minimal anthropogenic and

271   electrical interference at the site resulted in high-quality data. Final site interpretation was based

272   on rigorous CSAMT data processing, including skew filtering and curve analysis (Hasan et al.,

273   2025).

274   **2.2.3 Processing workflow**

275   Spatial filters (Hanning window) and static corrections were applied to refine resistivity data and

276   enhance the model accuracy. The static corrections addressed near-surface resistivity

277   inhomogeneities that cause vertical shifts in apparent resistivity curves. By calibrating electric

278   field measurements to a stable reference, shallow-layer effects were minimized, isolating deeper

279   signals. Spatial filtering using a Hanning window reduced high-frequency noise while preserving

280   coherent spatial patterns. This approach significantly improved inversion model stability by

281   suppressing spectral leakage and smoothing fluctuations. Data processing was carried out using

282   the CMTPro version software produced by Phoenix Geophysics (Phoenix Geophysics CMTPro,

283   2020), which integrates V8 and tracking data, corrects coordinates, smoothes curves, and exports

284   files for inversion. Based on CSAMT-SW technique, the processing workflow shown in Fig. 2

14

285   (Phoenix Geophysics CSAMT-SW, 2020) was conducted to obtain 2D inversion (Rodi and

286   Mackie, 2001; Wang et al., 2015).
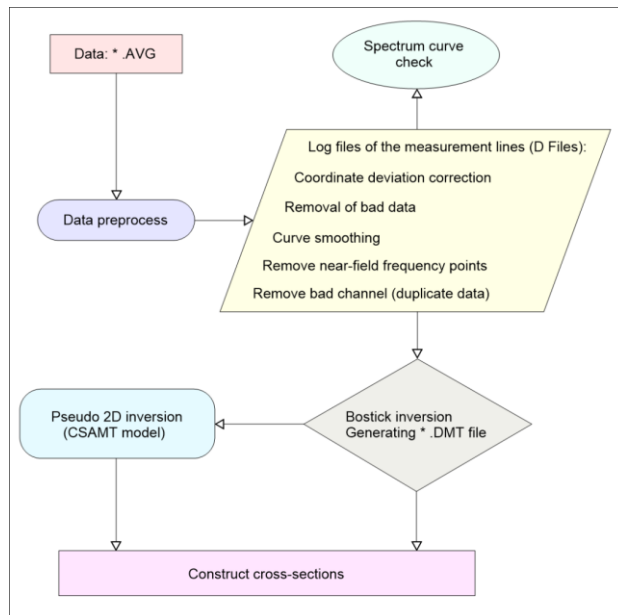
287

288   **Fig. 2.** Schematic of the 2D CSAMT data inversion workflow using Bostick methodology

289   The main components of the CSAMT-SW framework are: 1. Transformation from AVG

290   to D format; 2. Editing CHK data and converting to D format; 3. Manual data checks: gap filling,

291   near-field removal; 4. Smoothing based on D-format data; 5. Estimation of correction factors (D,

292   H, K, Z); 6. The Bostick inversions; 7. The Quasi-2D inversions using the global field model

293   (ID), integrating near and transition fields. Post-Bostick inversion results were stored as

294   *_BOS.DAT and *_BSS.DAT, with final inversion-ready data in *_M.DMT. The 2D inversion

295   proceeded until either the RMS error threshold or a five-iteration limit was reached. Final

296 resistivity models (Fig. 3) were cross-validated with local geology and clearly delineated

297 subsurface features, offering a robust interpretation framework.

298
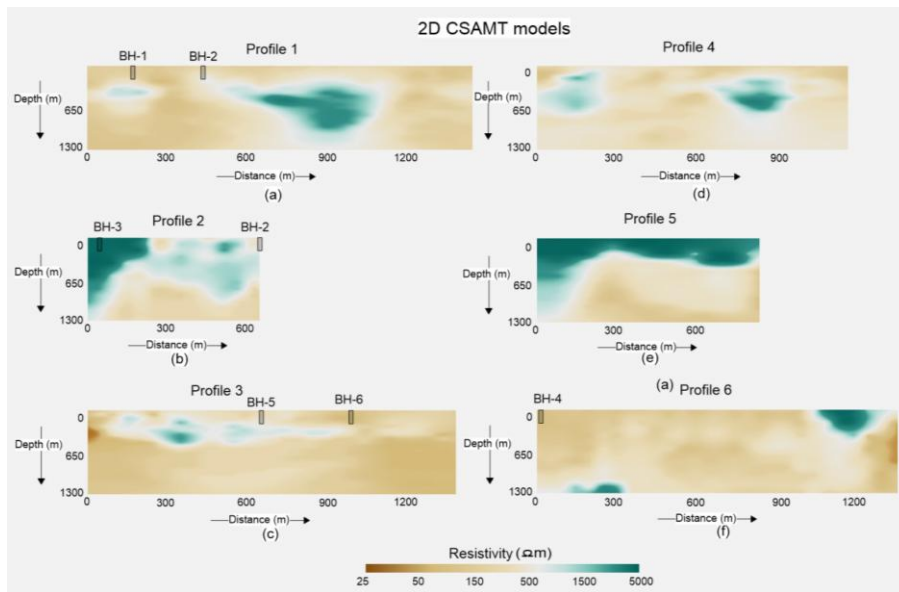
Fig. 3. Construction of 2D CSAMT models along six geophysical surveyed lines: (a) Line 1, (b) Line 2,

300 (c) Line 3, (d) Line 4, (e) Line 5, and (f) Line 6. Resistivity values increase from brown to green on the

301 color scale.

302 **2.3 Permeability estimation framework**

303 **2.3.1 Laboratory-based permeability determination from borehole core samples**

304 Permeability is a key hydrogeological parameter that quantifies the ability of porous media, such

305 as rock or sediment, to transmit fluids. It governs subsurface fluid flow and plays a central role in

306 groundwater studies (Allègre et al., 2016; Fiandaca et al., 2018; Mudunuru et al., 2022;

307 Esmaeilpour et al., 2023; Carbillet et al., 2024). Permeability reflects how easily fluids move

16

308 through pore networks or fractures and is typically measured via pumping tests or core analysis,

309 methods that are costly and logistically intensive. It is influenced by porosity, lithology,

310 saturation, structural features (e.g., faults, joints), and diagenetic processes (Dewandel et al.,

311 2006; Yan et al., 2024).

312   In this study, initial k data from the Jinji region were limited to six boreholes. To

313 strengthen the dataset, 116 lab tests were conducted on core samples from three main lithologies,

314 sandstone (31), hornstone (23), and granite (62), recovered from depths up to 200 m. These data

315 help delineate vertical k trends and refine the region's hydrogeological model. Core recovery

316 employed a wireline rotary system with triple-tube barrels to preserve sample integrity (ISRM,

317 2015). Samples were vacuum-sealed and stored under controlled humidity to retain in-situ

318 moisture and fracture structure. Prior to testing, cores were trimmed to standard 50 mm ×

319 100 mm cylinders and screened for visible defects. Two laboratory methods were used based on

320 k range. The steady-state flow test with ASTM D5084-21 guidelines (ASTM, 2021) was applied

321 to higher-k sandstone. A constant hydraulic gradient was applied under fully saturated

322 conditions, and the corresponding volumetric flow rate was recorded. Permeability was

323 determined through the application of Darcy's Law:

324 $$k = \frac{Q \cdot \mu \cdot L}{A \cdot \Delta P} \qquad (1)$$

325 where ΔP is the pressure differential applied across the sample (Pa), A is the cross-sectional area

326 (m²), L is the length of the sample (m), μ is the dynamic viscosity of the fluid (Pa·s), and Q is the

327 volumetric flow rate (m³/s).

328   For low-k hornstone and granite, the pulse decay method (Brace et al., 1968) was used. A

329 brief pressure pulse was applied, and pressure decay was monitored under confining stresses up

17

330 to 30 MPa to simulate in-situ conditions and assess stress-dependent k behavior. Tests were

331 conducted under both dry and saturated conditions to evaluate moisture sensitivity. Replicate

332 measurements ensured data reliability, and statistical analyses assessed intra- and inter-lithology

333 variability. Results revealed that granite had the lowest k due to its dense crystalline structure,

334 while hornstone showed intermediate values, likely due to localized fracturing. Sandstone

335 exhibited the highest k, particularly at greater depths, confirming its role as the primary aquifer

336 unit in the region.

337 **2.3.2 Permeability-resistivity relationship: Archie's law and the role of Kozeny–Carman**

338 Numerous foundational studies have linked electrical resistivity to hydraulic properties like k. A

339 prominent example is the Archie equation (Archie, 1942), which relates resistivity to porosity

340 and water saturation in clean, saturated sediments. However, its assumption of clay-free

341 conditions limits its applicability in complex or clay-rich lithologies (Waxman and Smits, 1968;

342 Glover, 2015). It is commonly expressed as:

343
$$\rho b = a \cdot \rho f \cdot \phi^{-m} \qquad (2)$$

344 In this equation, ϕ is porosity, ρf is fluid resistivity, ρb is bulk resistivity, and a and m are

345 empirical constants. Although Archie's law does not directly yield k, porosity serves as a useful

346 proxy due to its strong influence on fluid movement. As such, the resistivity–porosity

347 relationship can be leveraged to infer k indirectly, especially when supplemented with additional

348 petrophysical frameworks (Revil and Cathles, 1999).

349   The Kozeny–Carman equation, though not used explicitly in this study, provides a widely

350 accepted theoretical foundation that connects k to porosity and specific surface area (DallaValle,

351 1956; Bear, 1972). While it does not incorporate resistivity directly, this model is often used in

18

352 hydrogeophysical studies to support the interpretation of petrophysical relationships that bridge

353 electrical and hydraulic properties (Chapuis and Aubertin, 2003). Its relevance lies in the broader

354 theoretical justification for using porosity, derived or inferred from resistivity, as a predictor of k.

355 The application of this equation alongside Archie's law facilitates the development of empirical

356 or semi-empirical models that connect electrical resistivity to k (Glover, 2009; Yan et al., 2024).

357 However, direct application of these equations to complex geological environments, such

358 as fractured granite, sandstone, and hornstone, remains limited due to heterogeneities in mineral

359 composition, pore connectivity, and structural anisotropy. To mitigate such constraints, our

360 approach empirically develops a localized, site-calibrated correlation involving k and resistivity,

361 grounded in co-located deep borehole and CSAMT data. This empirical link supports high-

362 resolution spatial modeling of k in both 2D and 3D for the Jinji area, offering enhanced insight

363 into subsurface hydrogeological conditions where traditional models may not be applicable.

364 **2.3.3 Spatial permeability modeling from CSAMT data**

365 To estimate permeability across the entire study area, we employed a multi-stage approach

366 integrating borehole core analysis with CSAMT-derived resistivity data. In the first stage, a total

367 of 116 laboratory-based k measurements were acquired using 6 drilling tests (from BH-1 to BH-6)

368 with 0–200 m depth (Fig. 4). The k measurements were obtained from intact rock core samples

369 representing three principal lithologies: granite, hornstone, and sandstone.

370 In the second stage, each of the 116 borehole-derived k values was empirically correlated

371 with corresponding resistivity values extracted from CSAMT soundings co-located with the

372 borehole sites. The spatial correspondence between boreholes and CSAMT sounding points was

373 carefully matched (Fig. 4). For example: P1-5 represents the fifth CSAMT sounding at 200 m

374 along survey line 1 near borehole BH-1; P1-9 corresponds to the ninth sounding at 400 m on line

375 1 near borehole BH-2; P2-3 denotes the third sounding at 100 m along line 2 near BH-3; P6-1

376 indicates the first sounding at 0 m on line 6 adjacent to BH-4; P3-15 and P3-21 represent the

377 fifteenth (700 m) and twenty-first (1000 m) soundings along line 3, near boreholes BH-5 and

378 BH-6, respectively.
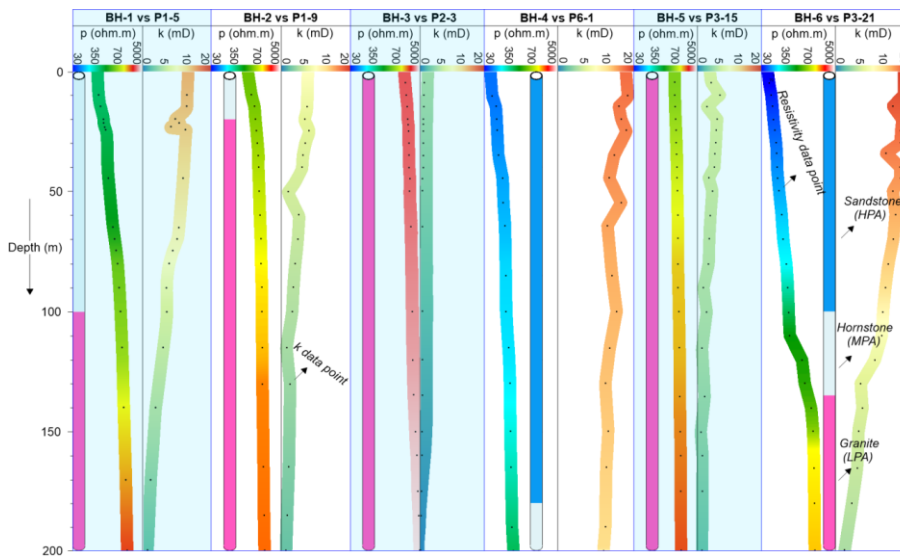
379

380 **Fig. 4.** Comparison of 116 CSAMT-based resistivity (ρ) data points with corresponding drilling-based

381 permeability (k) values at depths of 0–200 m across six borehole locations (BH-1 to BH-6). The data were

382 used to evaluate high potential aquifers (HPA) in sandstone, medium potential aquifers (MPA) in

383 hornstone, and low potential aquifers (LPA) in granite. Each dot represents a resistivity or permeability

384 data point. Sounding labels indicate specific CSAMT locations: P1-5 (5th point on line 1), P1-9 (9th on

385 line 1), P2-3 (3rd on line 2), P6-1 (1st on line 6), and P3-15 and P3-21 (15th and 21st on line 3)

386   In the third stage, all 116 paired measurements of k and ρ were utilized to develop an

387   empirical model. An exponential relationship was derived between permeability (k in

388   millidarcies or mD) and electrical resistivity (ρ in Ωm), expressed as follows (Fig. 5):

389    $$k = 15.373\, e^{-0.002\rho} \qquad (3)$$

390   This site-specific empirical model was then applied to the entire suite of CSAMT resistivity data

391   collected along six survey profiles to estimate spatial variations in k across the broader study area.

392   Using this relationship, we generated predictive 2D and 3D k models that capture the hydraulic

393   behavior of three major lithological units: low potential aquifer (LPA): associated with low-

394   permeability granite, medium potential aquifer (MPA): hosted within fractured hornstone

395   (hornfels), high potential aquifer (HPA): corresponding to more porous sandstone units.

396   These models provide a depth-resolved assessment of subsurface k reaching depths of up

397   to 1300 m below the surface. Final 2D and 3D spatial visualizations were developed by SKUA-

398   GOCAD and Geosoft Oasis montaj modeling software (Webring, 1981; Mira Geoscience Ltd.,

399   1999; Hasan et al., 2024), enabling the visualization of k distributions across all six CSAMT

400   profiles and improving hydrogeological characterization in structurally complex hard rock terrain.

401
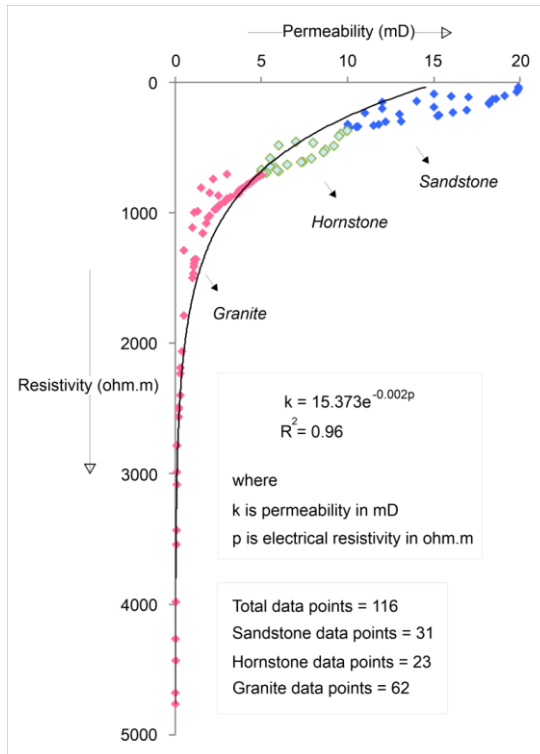
Fig. 5. Empirical relationship derived from 116 data points comparing CSAMT-based resistivity and drilling-based k at depths of 0–200 m, across three lithologies: sandstone (31 data points), hornstone (23 data points), and granite (62 data points).

3 Results

3.1 Cross-validation of geophysical and borehole parameters

Table 2 summarizes the integrated dataset from 6 drills and 6 geophysical profiles to resolve the spatial structure of the subsurface into three distinctive hydrogeological units, based on variations in electrical resistivity and corresponding k values. The development of these

22

410   subsurface models mainly depends on borehole data, CSAMT-derived resistivity measurements,

411   and the regional geological framework. The stratigraphy was categorized into three primary

412   lithologies: sandstone, hornstone, and granite. Classification criteria were established as follows:

413   sandstone was defined by resistivity values below 350 Ωm and a k range of 10–20 mD;

414   hornstone exhibited resistivity values between 350 and 700 Ωm with a k range of 5–10 mD; and

415   granite was characterized by resistivity values exceeding 700 Ωm and k values ranging from 0 to

416   5 mD. Based on our evaluations of the subsurface hydrogeological model's aquifer potential

417   zones, we found that sandstone contains the high potential aquifer (HPA), hornstone contains

418   medium potential aquifer (MPA), and granite has low potential aquifer (LPA). Aquifers with the

419   largest yields or the best water-bearing capacity are indicated by sandstone, whereas aquifers

420   with the lowest yields or the worst water-bearing capacities are denoted by granite. Groundwater

421   development is best facilitated by sandstone in the study area, whereas groundwater extraction is

422   most hindered by granite.

423   **Table 2**

424   Integrating distinct ranges of electrical resistivity and k enables a comprehensive assessment of

425   groundwater potential across various hard rock types

Resistivity (Ωm)	k (mD)	Type of rock	Aquifer potential
< 350	10–20	Sandstone	High potential aquifer (HPA)
350–700	5–10	Hornstone	Medium potential aquifer (MPA)
>700	0–5	Granite	Low potential aquifer (LPA)

426   **3.2 2D groundwater assessments**

23

427　Using geophysical-borehole correlation as its basis, Eq. (3) efficiently converts 2D CSAMT

428　models (Fig. 3) into 2D k models (Fig. 6). The interpreted 2D k models shown in Fig. 7, in

429　comparison with the limited borehole experiments, allow for a comprehensive assessment of the

430　groundwater resources in hard rock across the whole research area, from 0 to 1300 m deep.
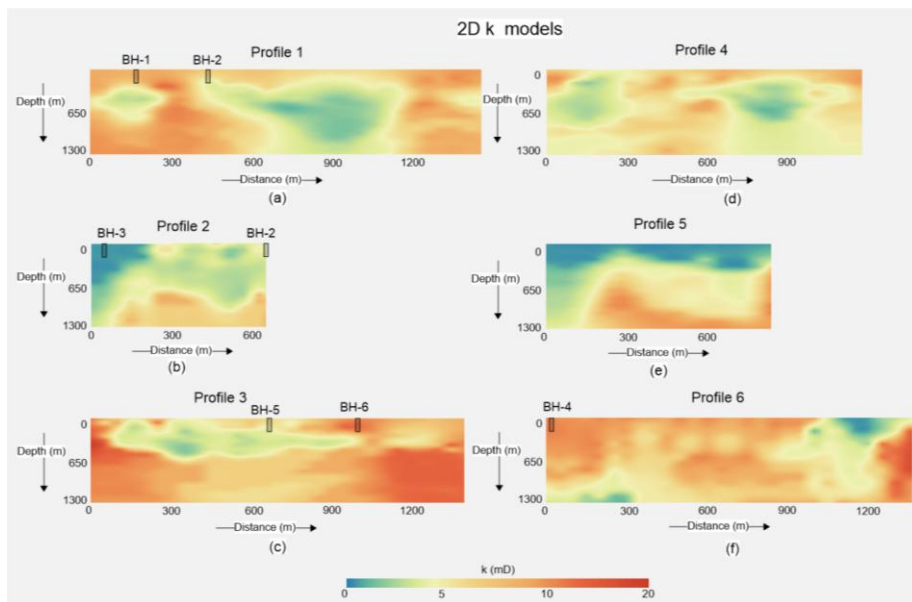
431

432　**Fig. 6.** The predicted 2D k models along six geophysical surveyed lines: (a) Line 1, (b) Line 2, (c) Line 3,

433　(d) Line 4, (e) Line 5, and (f) Line 6. k values increase from blue to red on the color scale.
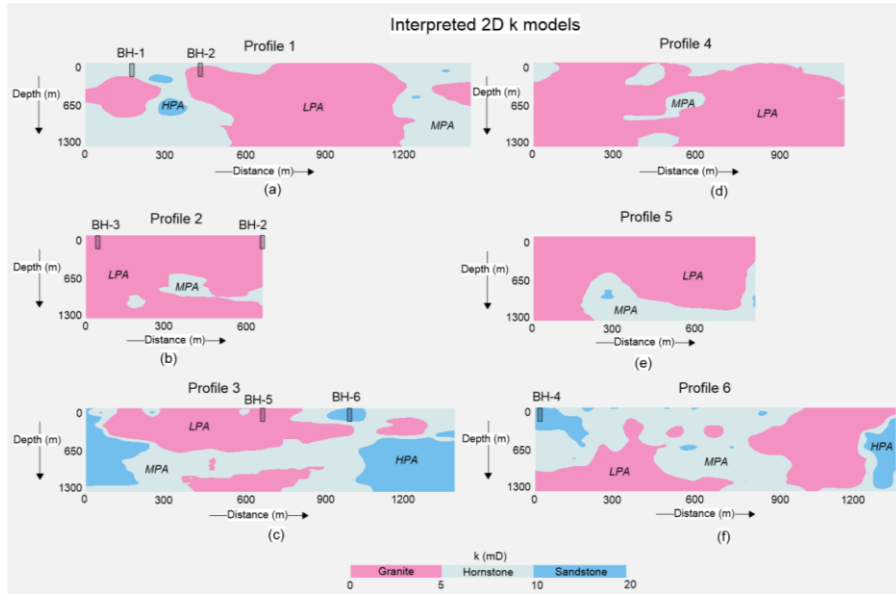
Fig. 7. The interpretation of the predicted 2D k models along six geophysical surveyed lines: (a) Line 1, (b) Line 2, (c) Line 3, (d) Line 4, (e) Line 5, and (f) Line 6. Sandstone is represented in blue, hornstone in light blue, and granite in pink

The integrated 2D k models (Fig. 8) and their interpretations (Fig. 9) provide a detailed evaluation of groundwater potential across complex geological settings of sandstone, hornstone, and granite. Profile 1 reveals a high-potential sandstone aquifer (85–305 m thick) between 245–380 m distances at 205–400 m depth. Medium-potential hornstone aquifers are found from 0–525 m and 1185–1445 m distance down to 1300 m. Low-potential granite aquifers appear at 0–285 m (290–790 m depth), 385–1185 m (full depth), and 1305–1450 m (390–745 m depth). Profile 2 shows a medium-potential hornstone aquifer with 140–380 m thickness (490–1105 m depth) between 145–215 m and 290–645 m distance. No high-potential sandstone aquifers are present. Granite dominates (0–700 m distance, 0–1300 m depth) the profile with low yield except

25

447   in hornstone zones. Profile 3 contains both high-potential sandstone (0–250 m, 905–1065 m, and

448   1040–1390 m distances at respective depths of 0–1190, 0–205, and 490–1305 m) and medium-

449   potential hornstone aquifers (full depth with 0–1400 m distance) across the entire surveyed line.

450   Granite aquifers are assessed at 80–1015 m (0–590 m depth), 395–845 m (915–1300 m depth),

451   and 1100–1300 m (200–500 m depth). Profile 4 features medium-potential hornstone at 0–105 m

452   (0–340 m depth), 340–645 m (0 to 1300 m depth), 595–790 m (0–300 m depth), and 1015–1145

453   m (0–345 m depth). No high-potential sandstone is observed. Granite aquifers of low potential

454   dominate (0–1145 m distance between 0–1300 m depth), except in hornstone zones. Profile 5

455   shows medium-potential hornstone (190–845 m distance, 390–1300 m depth) and two small

456   high-yield sandstone patches (290 m at 790–960 m depth and 815 m at 1045–1135 m depth).

457   Low-potential granite appears at distance 0–190 m (0–1300 m depth) and 790–815 m (0–1025 m

458   depth). Profile 6 includes high-potential sandstone zones at 0–190 m (0–490 m depth) and 1245–

459   1345 m (215–1225 m depth). Low-potential granite is present at 0–690 m (390–1300 m depth)

460   and 790–1360 m (0–1190 m depth), while hornstone with medium potential dominates the

461   remainder. Overall, the southeastern and northwestern zones host abundant medium- to high-

462   potential aquifers, while central regions show limited or poor groundwater prospects.

463
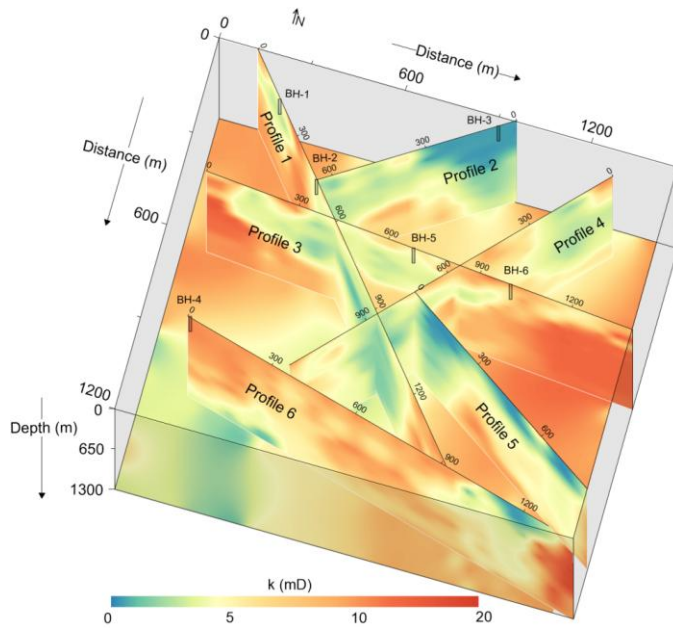
Fig. 8. The integrated 2D *k* models derived from the incorporation of geophysical and drilling data, with *k*

represented on a color bar spanning from green to red

466

k (mD)

| Granite | Hornstone | Sandstone |

0   5   10   20
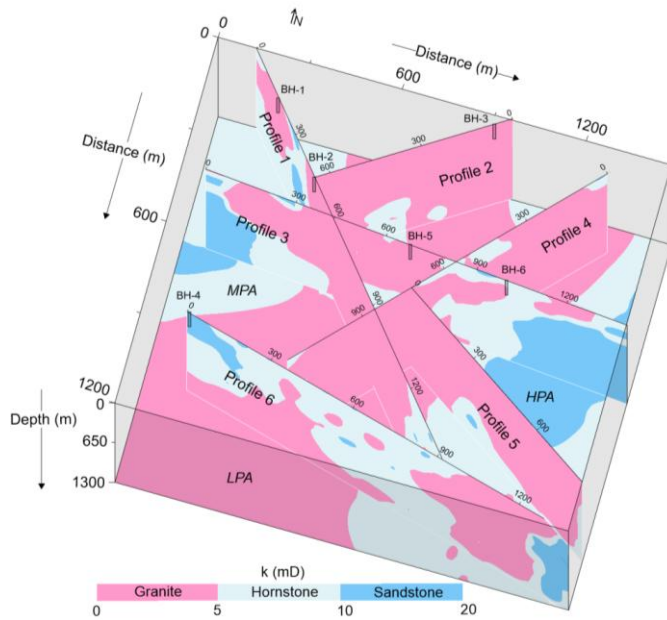
Fig. 9 Analysis of 2D *k* models, based on defined *k* ranges, for three groundwater potential aquifers: low

potential aquifer (LPA), medium potential aquifer (MPA), and high potential aquifer (HPA),

corresponding to the granite, hornstone, and sandstone formations, respectively

3.3 3D groundwater assessments

The 3D *k* (outer view) visualization (Fig. 10a, b) provides a comprehensive assessment of the

water-bearing capacity of the rock mass. Low-potential granite aquifers are found at the surface

along: line 1 (85–215 m, 385–1175 m), line 2 (0–655 m), line 3 (0–45 m, 95–175 m, 265–585 m,

605–845 m, 1145–1315 m), line 4 (90–390 m, 490–615 m, 745–1115 m), line 5 (0–815 m), and

line 6 (1045–1345 m). Medium-potential hornstone aquifers appear along: line 1 (0–95 m, 190–

260 m, 295–415 m, 1185–1425 m), line 3 (40–105 m, 215–275 m, 580–605 m, 850–910 m,

1010–1155 m, 1310–1410 m), line 4 (45–90 m, 390–490 m, 590–685 m, 1115–1185 m), and line

28

478   6 (90–190 m, 215–275 m, 315–485 m, 505–605 m, 635–1045 m). High-potential sandstone

479   aquifers are identified in: line 1 (265–310 m), line 3 (235–255 m, 915–1010 m), line 4 (0–45 m),

480   and line 6 (0–90 m, 210–225 m, 275–305 m, 515–525 m, 605–635 m), Overall, Fig. 10 (a, b)

481   shows that higher-yield aquifers are mainly concentrated in the southern portion of the

482   investigated site.
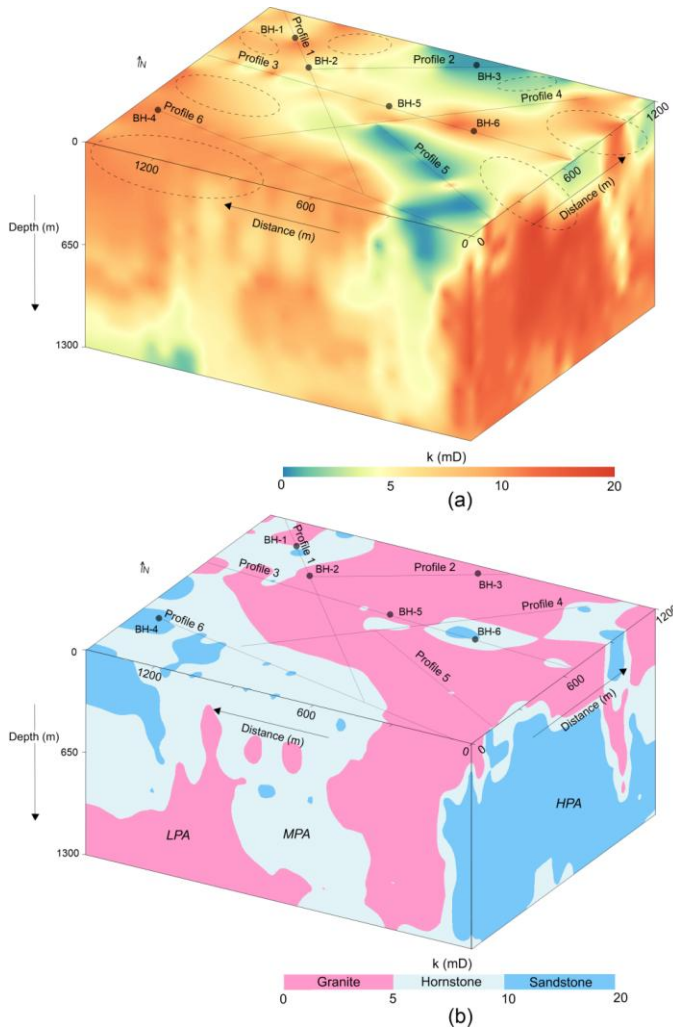
483

484 **Fig. 10.** The 3D k models (CSAMT-based), with k shown on a color scale increasing from green to red,

485 correspond to three groundwater potential aquifers: low potential aquifer (LPA), medium potential aquifer

486 (MPA), and high potential aquifer (HPA), associated with three geological strata: granite, hornstone, and

487 sandstone, respectively. The uncertainty contours (highlighted by areas with black dots) indicate zones of

488 reduced confidence in k estimation. (a) The exterior visualization of the 3D k model, and (b) The analysis

489 of the 3D k model from an external perspective

490 Fig. 11 (a, b) shows a 3D internal view of aquifer potential at 1300 m depth. Low-yield

491 granite aquifers are identified along: surveyed line 1 (515–1215 m), line 2 (0–290 m), line 3

492 (390–690 m), line 4 (0–1145 m), line 5 (0–195 m, 565–595 m), and line 6 (0–690 m, 1075–1115

493 m). Medium-potential hornstone aquifers are found along: profile 1 (0–540 m, 1215–1445 m),

494 profile 2 (295–675 m), profile 3 (175–395 m, 445–815 m, 915–1035 m), profile 5 (205–565 m,

495 610–815 m), profile 6 (685–1080 m, 1110–1355 m). High-potential sandstone aquifers appear

496 along: profile 3 (0–205 m, 1010–1400 m) and profile 5 (810–815 m). Overall, medium to high

497 potential aquifers are mainly distributed in the southeastern and northwestern regions, while

498 central areas are dominated by low-yield granite. The aerial 3D k model enhances visualization

499 of aquifer distribution, supporting accurate groundwater assessment.

30

(a)

(b)

500
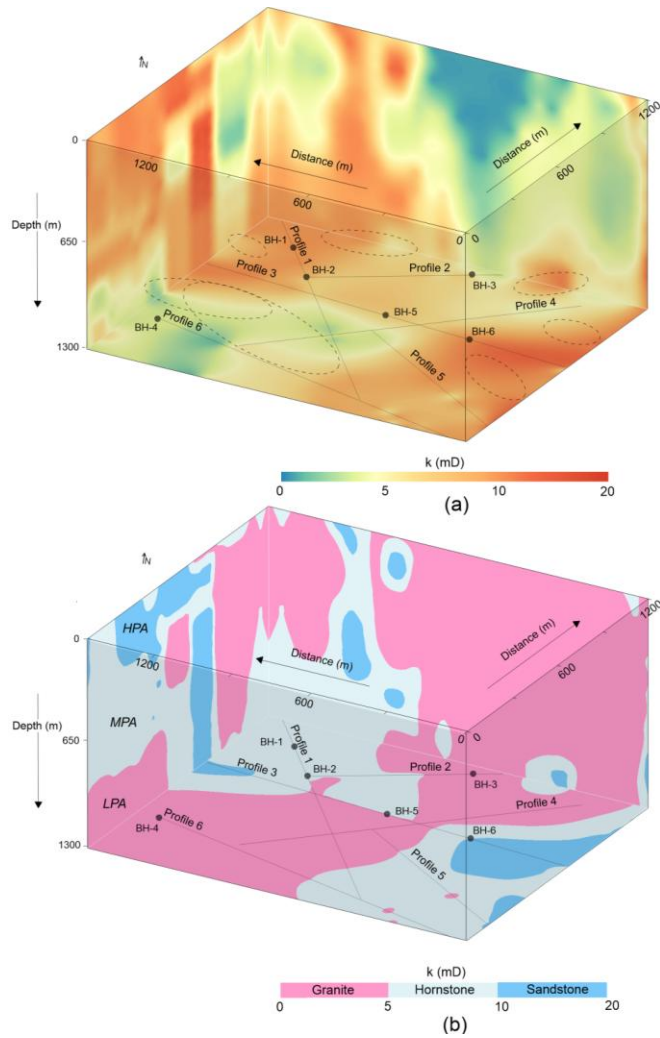
Fig. 11. The 3D *k* models (CSAMT-based), with *k* represented on a color scale ranging from green to red,
illustrate three groundwater potential aquifers: low potential aquifer (LPA), medium potential aquifer
(MPA), and high potential aquifer (HPA), associated with three geological strata: granite, hornstone, and
sandstone, respectively. The uncertainty contours (highlighted by areas with black dots) indicate zones of

31

reduced confidence in k estimation. (a) The interior visualization of the 3D k model, and (b) The analysis

of the 3D (internal perspective) k model

3.4 Depth-wise groundwater assessments

Due to limited borehole data, direct estimation of k below 200 m is not feasible.

However, by integrating borehole and CSAMT data, k values could be reliably estimated down

to 1300 m. This approach enabled efficient and detailed evaluation of hard rock aquifers using

both 2D and 3D models (Fig. 12), with k values extracted at depths of 0, 200, 600, 1000, and

1300 m. At 1300 m, over 42% of the subsurface in the southwest and northeast comprised low-

yield granite. Hornstone accounted for 40% (medium yield) near granite zones in the northwest

and southeast, while high-yield sandstone made up 18% in the east. At 1000 m, sandstone (15%)

was concentrated in the southeast (high yield), hornstone (38%) in the southeast and northwest

(medium yield), and granite (47%) dominated the central and boundary zones (low yield). At

600 m, the subsurface was 55% granite (central and northern zones, low yield), 32% hornstone

(western region, medium yield), and 13% sandstone (southeast, high yield). At 200 m, granite

dominated 64% of the center and north (low yield), hornstone made up 26% in the south

(medium yield), and sandstone (10%) in the west was associated with high yield. At 0 m, 73% of

the central area comprised low-yield granite, 20% of the southwest was hornstone (medium

yield), and 7% sandstone (high yield) was concentrated in the southwest.

Overall, Fig. 12 shows a decrease in low-yield granite thickness with depth. Groundwater

potential is lowest around 600–700 m depth, while deeper zones (>700 m) in the northwest,

southeast, and southwest show more favorable aquifer conditions.

32

526
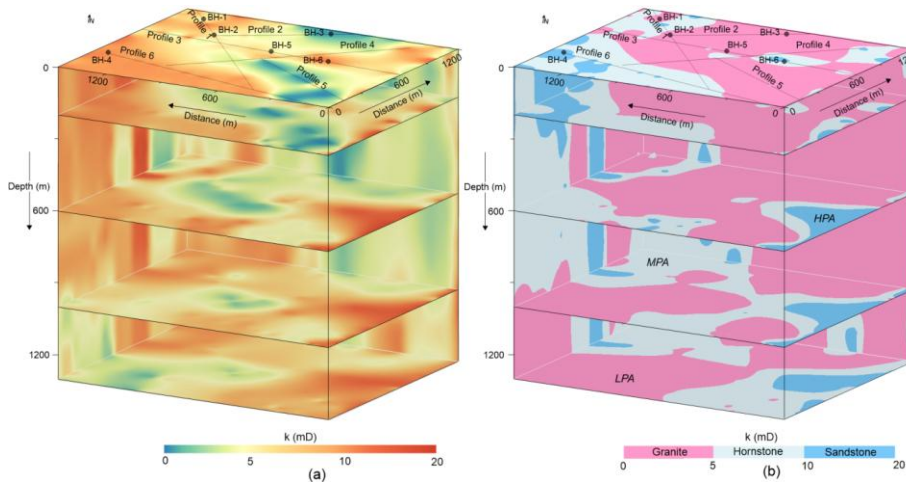
Fig. 12. (a) Geophysical *k* imaging at depths of 0, 200, 600, 1000, and 1300 m, with *k* shown on a color

scale increasing from green to red. (b) Evaluation of CSAMT-derived *k* values (based on defined *k* ranges)

at various depths for different aquifer types: low potential aquifer (LPA) in granite, medium potential

aquifer (MPA) in hornstone, and high potential aquifer (HPA) in sandstone

3.5 Validation of predicted vs. measured permeability

Groundwater evaluation was greatly improved by systematic CSAMT-based *k* estimation using

Eq. 3. As shown in Figs. 6–12, granite dominates the central, northeastern, and southwestern

zones; hornstone occurs mainly in the southeast, west, and northwest; and sandstone is prevalent

in the east. Borehole-based assessments are limited by inconsistent subsurface mapping. While *k*

values align near 200 m depth, broader extrapolation remains uncertain, highlighting the

limitations of sparse drilling in complex geology.

To clarify the basis of the percentage matching values, the following explicit equation

was used to quantify the agreement between CSAMT-derived *k'* values and borehole-based *k*

estimates:

33

$$\text{Percentage Match} = \left(\frac{\min(k, k')}{\max(k, k')}\right) \times 100 \qquad (4)$$

Here, min (k, k') is the smaller of the two permeability values, either the measured permeability (k) from borehole data or the estimated permeability (k') from the CSAMT model, at a given depth. Conversely, max (k, k') is the larger of the two values. This ratio offers a normalized agreement metric, where 100% indicates a perfect match and lower values reflect greater divergence. Table 3 summarizes results for 18 representative data points (out of 116 total calibration points). Percentage matches range from 30% to 100%. Higher agreement is generally observed in moderate-resistivity formations, whereas lower matches occur primarily in highly resistive, low-permeability granite units (e.g., BH-3), where small absolute differences produce larger relative deviations. Despite local discrepancies, both predicted and measured values consistently classify the same aquifer potential zones.

Because the empirical model was derived from 116 paired measurements, predictive capability was evaluated using leave-one-point-out cross-validation (LOOCV). Each observation was excluded sequentially; the regression was recalibrated using the remaining 115 data points; and permeability was predicted for the excluded point. Prediction error was quantified using the root mean square error (RMSE):

$$\text{RMSE} = \sqrt{\frac{1}{n}\sum_{i=1}^{n}(k_i - k'_i)^2} \qquad (5)$$

where k_i denotes the measured permeability, k'_i represents the predicted value for the excluded observation, and n = 116 is the total number of paired resistivity–permeability data points used in the cross-validation procedure. This procedure yielded:

$$\text{RMSE}_{\text{LOOCV}} = 2.36 \text{ mD} \qquad (6)$$

562 Given the observed permeability range (0.01–19.9 mD), this error indicates stable predictive

563 performance within the calibration domain. For the representative points listed in Table 3,

564 LOOCV-predicted permeability values differ only slightly from those obtained using the full

565 regression model, indicating that the fitted relationship is not strongly influenced by individual

566 observations.

567   To further assess spatial transferability, a leave-one-well-out cross validation was

568 conducted. In this approach, all data from one borehole were excluded, the regression was

569 recalibrated using the remaining wells, and permeability was predicted for the omitted well.

570 Using the same RMSE formulation (Eq. 5), this yielded:

571
$$RMSE_{well} = 2.78 \text{ mD} \qquad (7)$$

572 The modest increase in error relative to pointwise LOOCV reflects geological heterogeneity

573 rather than model instability. This result demonstrates that the empirical resistivity–permeability

574 relationship generalizes reasonably well across different boreholes and lithological domains.

575   Together, percentage agreement, leave-one-point-out validation, and leave-one-well-out

576 validation demonstrate that the CSAMT-derived empirical model provides robust and

577 transferable permeability estimates within the measured range. Although localized deviations

578 occur, likely due to structural anisotropy and fracture-controlled flow, the regression is not

579 dominated by single data points or individual wells, supporting its application for regional-scale

580 groundwater assessment.

581 **Table 3**

582 Percentage match and deviation between the measured k and the predicted k' for 18 selected data points

583 out of the total 116

CSAMT data points (selected)			Drilling data			%Matching	Difference
CSAMT sounding number	Resistivity (Ωm)	Predicted k' (mD) using Eq. (3)	Borehole name	Depth (m)	Measured k (mD)	k' vs k	between k' and k
P1-5	392	7.0	BH-1	10	9.6	73	2.6
P1-5	515	5.5	BH-1	40	8.7	63	3.2
P1-5	1080	1.8	BH-1	170	1.8	100	0.0
P1-9	669	4.0	BH-2	20	5.0	80	1.0
P1-9	863	2.7	BH-2	60	3.5	77	0.8
P1-9	1354	1.02	BH-2	185	1.2	85	0.18
P2-3	2187	0.2	BH-3	10	0.3	67	0.1
P2-3	2988	0.04	BH-3	85	0.1	40	0.06
P2-3	4765	0.003	BH-3	200	0.01	30	0.007
P6-1	50	13.9	BH-4	15	19.9	70	6.0
P6-1	200	10.3	BH-4	100	12.0	86	1.7
P6-1	348	7.7	BH-4	180	9.9	78	2.2
P3-15	792	3.3	BH-5	30	4.1	80	0.8
P3-15	1157	1.5	BH-5	135	1.6	94	0.1
P3-15	1412	0.91	BH-5	200	1.07	85	0.16
P3-21	165	11.1	BH-6	45	18.2	61	7.1
P3-21	708	3.7	BH-6	165	5.0	74	1.3
P3-21	846	2.8	BH-6	180	2.0	71	0.8

584

585   **4 Discussion**

586 **4.1 Scalable geophysical approach for deep groundwater modeling**

587 The integration of geophysics into groundwater studies provides an efficient and scalable

588 substitute for borehole-based methods, especially in deep and geologically complex terrains.

589 While boreholes provide direct k data, their use is limited by cost, logistics, and sparse coverage.

590 Our study presents a robust framework for 2D and 3D k modeling beyond 1 km depth by

591 integrating CSAMT with borehole data in a lithologically diverse setting. This approach

592 addresses key challenges in areas with limited surface water and low-k granite near the surface,

593 revealing deeper fractured zones with higher groundwater potential in granite, hornstone, and

594 sandstone. These deep aquifer insights support China's national water security strategies and

595 inform sustainable groundwater management under climate stress.

596 **4.2 Ensuring data quality and model reliability**

597 To minimize uncertainty and enhance accuracy, we implemented a rigorous workflow

598 throughout data acquisition, processing, inversion, and modeling. For CSAMT, this included

599 careful survey planning, optimized electrode configurations, and the application of advanced

600 filtering and static shift corrections. Inversion was guided by multidimensional modeling

601 constrained by borehole-derived a priori information, improving resolution and mitigating non-

602 uniqueness. Permeability measurements were obtained under controlled laboratory conditions

603 using high-quality, undisturbed core samples from six boreholes, reducing discrepancies between

604 laboratory and field scales. These measures, together with integrated lithological data, enabled

605 the development of a robust k model suitable for reliable groundwater assessment across the

606 study area.

607 **4.3 Comparative advantages of CSAMT for deep hard rock aquifer characterization**

37

608 CSAMT, developed in the 1970s, remains uniquely valuable for deep subsurface exploration,

609 particularly in resistive and fractured hard rock environments. Its ability to image at

610 intermediate-to-deep depths (hundreds to over a thousand meters) with relatively high resolution

611 and controlled signal strength enhances its ability to delineate lithological contacts and fluid-

612 bearing formations where other resistivity methods (VES and ERT) may fall short. While

613 electromagnetic methods such as MT and TDEM are also capable of probing deep subsurface

614 structures, achieving comparable results in similarly complex hard rock settings presents notable

615 challenges. MT, which relies on natural variations in electromagnetic fields, can reach even

616 greater depths than CSAMT and has been successfully applied in regional-scale hydrogeological

617 investigations, such as identifying deep groundwater circulation paths in mountain systems

618 (Jiang et al., 2014) and tracing flow systems that recharge lowland aquifers (Gonzalez-Duque et

619 al., 2024).

620 As summarized in Table 1, MT provides exceptional penetration (tens of kilometers) but

621 has reduced resolution in the upper crust and is highly sensitive to cultural noise, limiting its

622 suitability for detailed k-modeling at the site scale. TDEM, while rapid and effective for

623 intermediate depths, suffers loss of sensitivity in highly resistive formations, making it less

624 effective for fractured granite and hornstone settings. In contrast, CSAMT's controlled-source

625 design and strong immunity to cultural noise provide a balance of depth penetration depth and

626 resolution well-suited for site-specific groundwater studies in hard rock terrains.

627 Thus, the comparative analysis (Table 1) underscores why CSAMT is the most

628 appropriate method for this study: it bridges the gap between large-scale regional techniques

629 (MT, TDEM) and shallow, high-resolution methods (VES, ERT), enabling robust 2D and 3D

630 hydrogeophysical modeling essential for evaluating deep aquifer potential.

4.4 Calibrated resistivity thresholds for lithological and hydraulic discrimination

We developed a robust empirical relationship between resistivity and k using 116 co-located data pairs, 62 from granite, 31 from sandstone, and 23 from hornstone, spanning 35–4,765 Ωm and 0.01–19.9 mD, respectively. The strong correlation ($R^2 = 0.96$) ensures reliable k prediction and minimizes lithological bias. The lithological classification derived from the resistivity–permeability relationship in this study is both geologically plausible and empirically supported by borehole data and field observations. Specifically, granite showed high resistivity (>700 Ωm) and low k (0–5 mD), hornstone had intermediate resistivity (350–700 Ωm) and moderate k (5–10 mD), and sandstone was marked by low resistivity (<350 Ωm) and higher k (10–20 mD). These ranges align with the distinct hydrogeological behaviors of each lithology under the site-specific structural and mineralogical conditions. The resistivity thresholds were selected through an integrated approach combining lithological logs from boreholes, established empirical resistivity values reported in the literature, and the geoelectrical contrasts identified in CSAMT profiles. For instance, the high resistivity of granite reflects its dense, low-porosity matrix and limited fluid content, whereas the lower resistivity of sandstone and hornstone corresponds to increased pore connectivity and higher saturation, often associated with structural features or thermal alteration. To ensure robust classification, the resistivity thresholds were calibrated using co-located borehole observations from multiple calibration sites and iteratively refined to maximize agreement between observed lithology and the modeled resistivity–permeability domains. While we acknowledge that resistivity can vary within a given lithology due to localized factors such as fluid saturation, mineral alteration, or fracture density, sensitivity analyses indicated that moderate adjustments to the threshold values had minimal impact on the overall lithological classification or the interpretation of k trends. This suggests that the chosen

654   thresholds are well-suited to the structurally complex Jinji area. Nevertheless, we emphasize that

655   these resistivity–permeability associations are localized and should be recalibrated to account for

656   site-specific conditions before use elsewhere. Although site-specific, the approach demonstrates

657   how minimal calibration data can support high-resolution 2D/3D k modeling in data-scarce

658   settings. Future studies could benefit from probabilistic classification schemes or machine

659   learning approaches to further refine lithological mapping in geologically heterogeneous terrains.

660   **4.5 Impact of lithological and measurement variability on the resistivity–permeability**

661   **relationship**

662   The fitted relationship between resistivity and k, as illustrated in Fig. 5, is shaped by several

663   factors, including the geological setting, lithological heterogeneity, data distribution, and the

664   accuracy of both measurements. The broad dynamic range in our dataset provides a strong basis

665   for identifying trends across the three dominant lithologies: sandstone, granite, and hornstone.

666   This broad range is especially beneficial for resolving low-k formations such as granite, where k

667   remains uniformly low and shows minimal fluctuation. In these settings, even large shifts in

668   resistivity translate to relatively small changes in k, resulting in a gently declining inverse

669   relationship. In contrast, at lower resistivity values (e.g., <1,000 Ωm) where k exceeds 2 mD,

670   small resistivity shifts result in larger changes in k, leading to a more scattered and nonlinear

671   correlation. This pattern is geologically realistic and reflects the inherent variability of fractured

672   and porous zones in complex lithologies.

673   **4.6 Model validation and predictive reliability**

674   Matching between measured and predicted permeability (k vs. k') was also rigorously validated

675   (Table 3). Among 18 selected points from boreholes, 10 showed a difference of less than 1 mD,

with only two exceeding 4 mD. Despite minor deviations, all points were accurately classified by lithology. This confirms the empirical model's reliability and its utility for regional-scale *k* prediction, even in areas lacking direct measurements. The geophysical model effectively compensates for sparse drilling data, offering a scalable and cost-effective tool for hydrogeological evaluation in hard rock terrains.

4.7 Limited and shallow borehole calibration

A key limitation of this study is the restricted depth range of the calibration dataset. The empirical resistivity–permeability relationship (Eq. 3) was derived from 116 core measurements between 0 and 200 m depth. Application of this relationship to depths approaching 1300 m therefore represents extrapolation beyond the calibrated interval.

To explicitly address this uncertainty, a probabilistic permeability–depth framework was implemented (Fig. 13). Rather than extending Eq. 3 deterministically, prediction uncertainty was propagated from the regression and progressively inflated beyond the 200 m calibration limit. Within the calibrated interval, permeability estimates remain relatively well constrained. Below 200 m, however, the 95% prediction intervals widen substantially, quantifying decreasing confidence with increasing depth.

Importantly, deep predictions remain conditioned by observed CSAMT resistivity trends and preserve the physically consistent monotonic decrease in permeability with increasing resistivity. Nevertheless, processes not captured by the shallow dataset, such as stress-dependent fracture closure, evolving fracture connectivity, and mechanical anisotropy, may modify permeability behavior at depth. While the probabilistic framework constrains extrapolation risk, it does not eliminate structural uncertainty. Deep borehole testing and stress-dependent hydraulic

41

698 measurements are therefore required to validate permeability predictions below the calibration

699 range.

4.8 Choice of core-based permeability measurements versus pumping tests

701 Although pumping tests are widely regarded as the standard method for estimating aquifer

702 permeability (k), they provide only bulk, large-scale averages of hydraulic conductivity over the

703 tested interval. Such measurements are useful for assessing overall transmissivity but lack the

704 spatial resolution required for detailed 2D or 3D geophysical modeling, where localized contrasts

705 in hydraulic properties are critical. The objective of this study was to capture subsurface

706 heterogeneity at scales compatible with CSAMT-derived resistivity. For this purpose, point-

707 specific k measurements were necessary to ensure that calibration data reflected the same

708 resolution and spatial variability represented in the geophysical models. Core samples, analyzed

709 at discrete depths, offered this localized control and provided a closer match to the spatial scale

710 of CSAMT blocks. Therefore, core-derived k values were used in lieu of pumping tests. While

711 this approach inevitably shifts the focus from bulk aquifer transmissivity to matrix- and fracture-

712 scale variability, it ensures that the calibration dataset is scale-compatible with resistivity

713 measurements, thereby improving the reliability of the empirical k–ρ relationship and supporting

714 more accurate heterogeneity mapping in crystalline terrains.

4.9 Scale effects in permeability estimation

716 In addition to depth-related extrapolation, permeability estimation in this study is influenced by

717 scale transition between centimeter-scale core measurements and tens-of-meter-scale CSAMT

718 inversions. Core plugs (50 mm × 100 mm) primarily capture intrinsic matrix permeability and

719 fractures intersecting the limited sample volume. In fractured crystalline systems, however,

42

hydraulic flow is governed by connected fracture networks whose representative elementary volume (REV) may exceed the dimensions of a core specimen. Individual cores may therefore not reach the REV of the fractured rock mass, leading to systematic underestimation of bulk hydraulic conductivity.

By contrast, CSAMT inversions resolve an effective bulk resistivity over ~50 × 50 m blocks, integrating matrix and fracture contributions across a much larger volume. The empirical k–ρ relationship thus links matrix-scale permeability measurements with block-scale electrical responses. The dispersion observed in Fig. 5 is therefore not merely statistical noise but a reflection of geological heterogeneity and scale-dependent flow processes.

For example, low k values from intact granite cores may correspond to CSAMT blocks intersecting fracture corridors that enhance effective permeability at the field scale. Conversely, cores intersecting localized fractures may yield elevated k relative to the surrounding bulk medium. Variability in cementation, fracture density, and stress-controlled aperture closure further contributes to scatter.

Bridging this scale gap requires intermediate-scale hydraulic constraints. Integration of packer testing, interval hydraulic testing, borehole geophysics, and pumping tests would help reconcile matrix-scale measurements with field-scale connectivity and better constrain the effective REV of the fractured system. Such multi-scale calibration would reduce uncertainty in empirical relationships and improve permeability modeling in structurally complex crystalline terrains.

4.10 Inflection in the resistivity–permeability relationship: a depth analogue

The empirical resistivity–permeability (k–ρ) relationship developed in this study exhibits a sharp decline in k with increasing resistivity and a clear inflection near 1,000 Ωm. This mirrors classic

43

743 depth–permeability (k–z) trends (e.g., Manning and Ingebritsen, 1999; Saar and Manga, 2004;

744 Ingebritsen and Manning, 2010), where k decreases exponentially at shallow depths and follows

745 a power-law pattern deeper down. However, unlike those models that use depth alone, our

746 resistivity-based approach captures additional controls such as lithology, porosity, fluid content,

747 and fracturing, making it a more localized and physically representative proxy, especially in

748 heterogeneous hard rock settings.

749 Depth was considered but not used as the primary variable due to strong lateral variations

750 in resistivity and k caused by geological complexity. For instance, in the Jinji area, surface

751 granite shows high resistivity and low k, consistent with standard crustal profiles. However,

752 deeper hornstone and sandstone units exhibit lower resistivity and higher k, contrary to typical

753 depth trends, likely due to localized faulting, thermal alteration, and contact metamorphism that

754 enhance fracture connectivity. The resemblance between our k–ρ curve and established k–z

755 models reinforces its physical validity. The observed transition near 1,000 Ωm may reflect a shift

756 from conductive, fractured zones to compact, resistive rock masses. While hybrid models

757 incorporating depth may be useful in future work, our resistivity-based method provides a more

758 reliable and site-specific approach for k estimation in structurally complex terrains.

759 **4.11 Salinity effects and uncertainty in deep fluid properties**

760 The influence of factors beyond lithology, particularly groundwater salinity, on CSAMT-derived

761 resistivity warrants careful consideration. Electrical resistivity is sensitive to porosity, fracture

762 density, mineral alteration, fluid saturation, and fluid resistivity (ρ_f). In this study, the empirical

763 k–ρ relationship was calibrated using core samples from 0–200 m across six boreholes under

764 predominantly fresh groundwater conditions. Regional hydrochemical data from the Geological

765 Survey of China (800–1000 m depth) consistently indicate low salinity, supporting the
766 assumption of fresh groundwater within the investigated interval. However, no direct fluid data
767 are available below ~1 km, and the assumption of fresh conditions at greater depths represents an
768 important model constraint.

769 To evaluate this uncertainty, a sensitivity analysis was performed. If fluid resistivity were
770 reduced by 50% due to increased salinity, formation resistivity would decrease proportionally,
771 resulting in higher inferred permeability values when substituted into Eq. (3). Because
772 permeability increases exponentially with decreasing resistivity in the fitted model, this effect is
773 nonlinear and resistivity-dependent. Specifically, halving ρ_f increases inferred k by
774 approximately a factor of 2 at 1000 Ωm, 7 at 2000 Ωm, and up to 18 at 3000 Ωm. These results
775 indicate that salinity effects are modest in low-resistivity formations but may significantly
776 influence permeability estimates in highly resistive deep crystalline units.

777 Accordingly, the permeability model should be interpreted as valid under the assumption
778 of predominantly fresh groundwater conditions and should not be generalized to saline deep
779 aquifers without recalibration. Future investigations should incorporate deep borehole fluid
780 sampling, downhole conductivity logging, and hydrochemical analyses to directly constrain fluid
781 resistivity and reduce salinity-related uncertainty in deep permeability predictions.

782 **4.12 Uncertainty from model extrapolation and edge effects**

783 The 3D permeability (k) model was constructed by interpolating between 2D CSAMT inversion
784 profiles calibrated with borehole-derived k values from six reference locations. Given the
785 limitations in survey geometry and computational cost, full 3D inversion of the resistivity data
786 was not feasible. Instead, we implemented a geostatistical framework using ordinary kriging,

45

787 which integrated cross-sectional profiles and applied the resistivity–permeability relationship

788 across the model volume. The interpolation was guided by variogram models tuned to reflect the

789 spatial continuity of lithological units and constrained by borehole control points, thereby

790 maintaining geological consistency. While this approach provides a volumetric representation of

791 k that highlights the distribution of permeable zones, its reliability is scale- and data-density

792 dependent. The model is most robust in the central areas where CSAMT lines intersect and are

793 directly supported by borehole data. In contrast, reliability diminishes in regions between widely

794 spaced profiles and toward the model edges and corners, where no direct constraints exist.

795 Sensitivity analyses, based on alternative variogram structures and comparisons with inverse

796 distance weighting, consistently revealed greater variability and uncertainty in these peripheral

797 zones.

798   To address this, uncertainty contours were added to Figs. 10 and 11, delineating areas of

799 higher and lower confidence. The black dots marking borehole and survey line positions serve as

800 reference anchors, making it clear that interpolation quality decreases with increasing distance

801 from these control points. As such, interpretations in boundary regions should be treated with

802 caution, particularly where model predictions extend beyond the convex hull of available data.

803 We emphasize that the current model provides a reliable first-order framework for k distribution

804 in the study area, but future improvements should prioritize denser CSAMT line coverage and,

805 where feasible, the use of full 3D inversion techniques. Such approaches would better capture

806 lateral continuity, minimize edge effects, and enhance confidence in the extrapolated 3D

807 structure.

808 **4.13 Limitations of storage characterization**

46

A complete aquifer assessment requires evaluation of both permeability and storage parameters, including specific yield, specific storage, and storativity. This study primarily focuses on delineating spatial variations in permeability (k), referred to here as hydraulic flow potential, using CSAMT-derived resistivity calibrated with borehole data. While this approach provides robust insights into transmissivity patterns and fracture-controlled flow pathways, it does not directly quantify aquifer storage capacity.

Permeability and storage represent distinct hydrogeological properties. High k zones do not necessarily imply high storage if fracture porosity is limited, and conversely, formations with significant porosity may exhibit substantial storage despite moderate permeability. Due to the absence of deep pumping tests, drawdown analyses, and detailed porosity logs, storage parameters could not be independently constrained. As such, the present results characterize relative transmissivity and hydraulic connectivity rather than total extractable groundwater volume.

To avoid overgeneralization, the model outputs should therefore be interpreted as indicators of flow potential rather than comprehensive groundwater resource capacity. Future studies should integrate Nuclear Magnetic Resonance (NMR) logging, borehole geophysical porosity tools, interval hydraulic testing, and aquifer-scale pumping tests to better constrain storage properties alongside permeability. Such multi-parameter characterization would enable more rigorous evaluation of sustainable yield and groundwater resource potential in fractured hard rock systems.

4.14 Optimizing borehole placement for CSAMT calibration

830   Borehole placement in this study was guided by geological mapping, hydrological relevance, and

831   preliminary CSAMT interpretation to ensure representative coverage of the principal lithologies

832   and structural domains. The six boreholes were used both to calibrate the empirical resistivity–

833   permeability relationship and to validate the CSAMT-derived permeability models. Cross-

834   validation results demonstrate that calibration quality depends more on spatial distribution than

835   on borehole number. Leave-one-out cross-validation (LOOCV) of the 116 paired measurements

836   yielded an RMSE of 2.36 mD, indicating that the regression is not overly sensitive to individual

837   data points. Leave-one-well-out cross-validation resulted in an RMSE of 2.78 mD, showing that

838   the empirical relationship maintains reasonable predictive capability when applied to an entirely

839   excluded borehole. The modest increase in error reflects geological heterogeneity rather than

840   model instability.

841   These findings suggest that a limited but strategically distributed set of boreholes across

842   key lithological and structural zones can provide stable calibration. Slightly higher prediction

843   errors in highly resistive granite highlight the importance of including structurally complex units

844   in calibration. Future work may further optimize efficiency by integrating preliminary CSAMT

845   results into adaptive drilling strategies, targeting areas of higher uncertainty while minimizing

846   drilling costs.

847   **4.15 Rationale for variable CSAMT profile extents**

848   The variation in CSAMT profile lengths reflects site-specific logistical and geological

849   constraints encountered during field deployment. Factors such as terrain accessibility,

850   infrastructure (e.g., roads, buildings), and the need to capture key geological features (e.g., faults,

851   lithological boundaries) influenced the extent of each profile. In some cases, shorter profiles

852   were required due to rugged topography or land access limitations, while longer profiles were

853   employed where feasible to ensure adequate coverage across broader structural domains. Despite

854   the variation in length, all profiles were designed to achieve sufficient ~~depth~~ penetration depth

855   and resolution for reliable resistivity–permeability modeling, as validated through borehole

856   calibration.

4.16 Addressing the borehole–CSAMT depth discrepancy

858   The borehole data used for calibration were limited to 0–200 m depth, whereas the CSAMT-

859   derived permeability model extends to approximately 1300 m. This vertical discrepancy reflects

860   practical drilling limitations rather than conceptual inconsistency. The shallow calibration

861   interval encompasses the principal lithologies (granite, hornstone, and sandstone) and captures a

862   representative range of resistivity–permeability conditions required to establish the empirical

863   relationship (Eq. 3).

864   Application of this relationship at greater depths constitutes extrapolation beyond the

865   calibrated interval, and the associated uncertainty is explicitly treated through the probabilistic

866   depth framework (Section 4.7) and salinity sensitivity analysis (Section 4.11). These analyses

867   demonstrate that confidence decreases progressively with depth and that deep permeability

868   estimates remain conditional on assumptions regarding fracture continuity and fluid resistivity.

869   Despite the absence of direct deep borehole validation, the extrapolated model exhibits

870   spatial consistency with mapped lithological boundaries, structural trends, and regional

871   hydrogeological interpretations reported by the Geological Survey of China. This structural

872   coherence supports the plausibility of deeper projections, while acknowledging that they remain

873   less constrained than the shallow interval.

874   Future deep drilling, in-situ hydraulic testing, and petrophysical logging will be essential

875   to independently verify permeability estimates below 200 m and further reduce vertical

876   extrapolation uncertainty.

877   **4.17 Ground-truthing CSAMT with regional geological frameworks**

878   Our results show strong agreement with regional geological and hydrogeological data from local

879   and national surveys, confirming the reliability of the integrated CSAMT–borehole approach.

880   This alignment supports the method's scientific validity and scalability for k estimation in

881   structurally complex, data-scarce settings. While grounded in established geophysical principles,

882   the strength of this study lies in its site-specific integration of deep k modeling, field validation,

883   and empirical calibration. Overall, the findings highlight CSAMT's potential as a practical tool

884   for deep groundwater exploration and sustainable resource management.
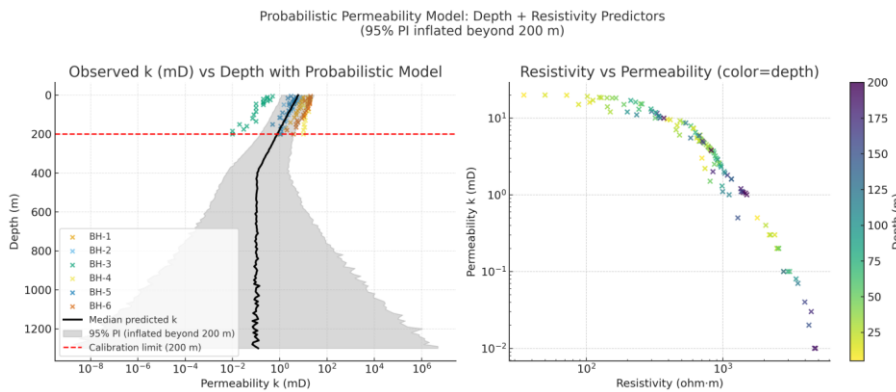
885

886   **Fig. 13**. Probabilistic permeability–depth model based on resistivity–permeability calibration from 116

887   borehole samples (0–200 m). The extrapolation to 1300 m shows increasing uncertainty with depth due to

888   limited calibration data.

5 Conclusions

This study introduces a novel, non-invasive methodology for deep groundwater investigation using CSAMT, applied for indirect estimation of 2D and 3D k distributions in complex hard rock terrains at depths reaching 1300 m. Conventional borehole drilling remains indispensable for direct hydraulic parameter evaluation, but its high cost and limited coverage restrict broader applicability. Our approach combines borehole calibration with CSAMT resistivity to establish an empirical k–ρ relationship, enabling the construction of spatially continuous hydrogeological models that extend beyond the reach of direct sampling.

It is important to note that the empirical relationship (Eq. 3) derived in this study is site-specific to the Jinji region's geological and hydrogeochemical conditions. Its constants should not be generalized to other regions without new calibration data. The key contribution of this work is therefore the methodology, a workflow for integrating CSAMT with borehole calibration, rather than the specific coefficients of the empirical equation. The resulting permeability models align well with lithological boundaries, revealing low-k granite zones (>700 Ωm, 0–5 mD) and high-k sandstone zones (<350 Ωm, 10–20 mD). Promising groundwater targets were identified below 700 m in central regions and around granite–sediment contacts, extending to depths of ~1300 m. While these results demonstrate the power of CSAMT for deep groundwater assessment, they remain dependent on the availability and quality of borehole data for calibration.

Future work should emphasize deep borehole validation, probabilistic modeling, and multi-scale integration to reduce uncertainty and improve confidence in permeability predictions. By coupling CSAMT with hydrochemical, porosity, and advanced logging data, this approach

911 can evolve into a robust and transferable framework for groundwater assessment in complex

912 hard rock terrains, while acknowledging inherent site-specific limitations.

913 **Code availability**

914 Software application or custom code supports the published claims and complies with field

915 standards

916 **Data availability**

917 Data available on request from the corresponding author

918 **Author contributions**

919 MH conceptualized the research goals and developed the methodology. MH and LS found the

920 funding for the project. MH developed the code and prepared its visualization, and LS provided

921 programming support and analysis tools. MH prepared the original draft.

922 **Declaration of competing interest**

923 The authors declare that they have no conflict of interest.

924 **Acknowledgements**

929 **Financial support**

References

1. Abbas, M., Deparis, J., Isch, A., Mallet, C., Jodry, C., Azaroual, M., Abbar, B., and Baltassat, J.M.: Hydrogeophysical characterization and determination of petrophysical parameters by integrating geophysical and hydrogeological data at the limestone vadose zone of the Beauce aquifer, Journal of Hydrology, 615, 128725, 2022. https://doi.org/10.1016/j.jhydrol.2022.128725.

2. Allègre, V., Brodsky, E.E., Xue, L., Nale, S.M., Parker, B.L., and Cherry, J.A.: Using earth-tide induced water pressure changes to measure in situ permeability: A comparison with long-term pumping tests, Water Resour. Res, 52(4), 3113–3126, 2016. https://doi.org/10.1002/2015WR017346.

3. Amiotte Suchet, P., Probst, J.L., and Ludwig, W.: Worldwide distribution of continental rock lithology: Implications for the atmospheric/ soil CO_2 uptake by continental weathering and alkalinity river transport to the oceans, Glob Biogeochem Cycles, 17, 1038, 2003. https://doi.org/10.1029/2002GB001891.

4. Archie, G.E.: The electrical resistivity log as an aid in determining some reservoir characteristics, Transactions of the AIME, 146(1), 54–62, 1942. https://doi.org/10.2118/942054-G.

952   5. Asfahani, J.: Estimation of the hydraulic parameters by using an alternative vertical
953   electrical sounding technique: case study from semiarid Khanasser valley region
954   Northern Syria, Acta Geophys, 71, 997–1013, 2023. https://doi.org/10.1007/s11600-022-
955   00926-0.

956   6. ASTM.: Standard Test Methods for Measurement of Hydraulic Conductivity of Saturated
957   Porous Materials Using a Flexible Wall Permeameter (ASTM D5084-21), ASTM
958   International, 2021. DOI: 10.1520/D5084-21.

959   7. Bauer-Gottwein, P., Gondwe, B.N., Christiansen, L., Herckenrath, D., Kgotlhang, L., and
960   Zimmermann, S.: Hydrogeophysical exploration of three-dimensional salinity anomalies
961   with the time domain electromagnetic method (TDEM), J. Hydrol., 380(3–4), 318–329,
962   2010. https://doi.org/10.1016/j.jhydrol.2009.11.007.

963   8. Bear, J.: Dynamics of Fluids in Porous Media. New York: American Elsevier Publishing
964   Company, 1972.

965   9. Binley, A., Cassiani, G., and Deiana, R.: Hydrogeophysics: opportunities and challenges,
966   Bollettino Di Geofisica Teorica Ed Applicata, 51(4), 267–287, 2010. [Online]. Available:
967   http://www.scopus.com/inward/record.url?eid=2-s2.0-
968   78650438167&partnerID=40&md5=96e14979c82f4b23e8fed0ac0140e7db.

969   10. Binley, A., Hubbard, S.S., Huisman, J.A., Revil, A., Robinson, D.A., Singha, K., and
970   Slater, L.D.: The emergence of hydrogeophysics for improved understanding of
971   subsurface processes over multiple scales, Water Resources Research, 51(6), 3837–3866,
972   2015. https://doi.org/10.1002/2015WR017016.

973 11. Borah, U.K., and Patro, P.K.: Estimation of the depth of investigation in the
974   magnetotelluric method from the phase, Geophysics, 84 (6), E377–E385, 2019.
975   https://doi.org/10.1190/geo2018-0124.1.

976 12. Brace, W.F., Walsh, J.B., and Frangos, W.T.: Permeability of granite under high pressure,
977   Journal of Geophysical Research, 73(6), 2225–2236, 1968.
978   https://doi.org/10.1029/JB073i006p02225.

979 13. Cagniard, L.: Basic theory of the magneto-telluric method of geophysical
980   prospecting, Geophysics, 18 (3), 605–635, 1953. https://doi.org/10.1190/1.1437915.

981 14. Carbillet, L., Griffiths, L., Heap, M.J., Duwiquet, H., Baud, P., Violay, M.E.S., Reuschlé,
982   T., and Guillou-Frottier, L.: The Influence of Micro- and Macrocracks on the
983   Permeability of Granite, Rock Mech Rock Eng, 58, 1361–1378, 2024.
984   https://doi.org/10.1007/s00603-024-04174-0.

985 15. Chapuis, R.P., and Aubertin, M.: Predicting the Coefficient of Permeability of Soils
986   Using the Kozeny-Carman Equation. E ´cole Polytech. Montre´al, 2003, [Online].
987   Available: http://publications.polymtl. ca/2605/

988 16. Condon, L.E., Markovich, K.H., Kelleher, C.A., McDonnell, J.J., Ferguson, G., and
989   McIntosh, J.C.: Where Is the Bottom of a Watershed? Water Resources Research, 56(3),
990   e2019WR026010, 2020. https://doi.org/10.1029/2019WR026010.

991 17. Daily, W., Ramirez, A., LaBrecque, D., and Nitao, J.: Electrical resistivity tomography of
992   vadose water movement, Water Resources Research, 28(5), 1429–1442, 1992.
993   https://doi.org/10.1029/91WR03087.

994   18. DallaValle, J.M.: Flow of Gases through Porous Media. P. C. Carman, Academic Press,
995   New York; Butterworths, London, 1956. 182 pp. Illus, 1956.
996   https://www.science.org/doi/10.1126/science.124.3234.1254.b.

997   19. Dell'Oca, A., Guadagnini, A., and Riva, M.: Interpretation of multi-scale permeability
998   data through an information theory perspective, Hydrol. Earth Syst. Sci., 24, 3097–3109,
999   2020. https://doi.org/10.5194/hess-24-3097-2020.

1000   20. Dewandel, B., Lachassagne, P., Wyns, R., Maréchal, J.C., and Krishnamurthy, N.S.: A
1001   generalized 3-D geological and hydrogeological conceptual model of granite aquifers
1002   controlled by single or multiphase weathering, Journal of Hydrology, 330(1–2), 260–284,
1003   2006. https://doi.org/10.1016/j.jhydrol.2006.03.026.

1004   21. Di, Q., Fu, C., An, Z., Wang, R., Wang, G., Wang, M., Qi, S., and Liang, P.: An
1005   application of CSAMT for detecting weak geological structures near the deeply buried
1006   long tunnel of the Shijiazhuang-Taiyuan passenger railway line in the Taihang Mountains,
1007   Engineering Geology, 268, 105517, 2020. https://doi.org/10.1016/j.enggeo.2020.105517.

1008   22. Esmaeilpour, M., Ghanbarian, B., Sousa, R., Peter, R., and King, P.R.: Estimating
1009   Permeability and Its Scale Dependence at Pore Scale Using Renormalization Group
1010   Theory, Water Resources Research, 59 (5), e2022WR033462, 2023.
1011   https://doi.org/10.1029/2022WR033462.

1012   23. Ferguson, G., McIntosh, J.C., Jasechko, S., Kim, J.H., Famiglietti, J.S., and McDonnell,
1013   J.J.: Groundwater deeper than 500 m contributes less than 0.1% of global river
1014   discharge, Communication Earth and Environment, 4, 48, 2023.
1015   https://doi.org/10.1038/s43247-023-00697-6.

1016 24. Fernando, A., and Pacheco, L.: Regional groundwater flow in hard rocks, Science of the

1017   Total   Environment,   506–507,   182–195,   2015.

1018   https://doi.org/10.1016/j.scitotenv.2014.11.008.

1019 25. Ferré, T., Bentley, L., Binley, A., Linde, N., Kemna, A., Singha, K., Holliger,

1020   k., Huisman, J.A., Minsley, B.: Critical Steps for the Continuing Advancement of

1021   Hydrogeophysics. Eos, Transactions American Geophysical Union, 90(23), 200, 2009.

1022   https://doi.org/10.1029/2009EO230004.

1023 26. Fiandaca, G., Maurya, P.K., Balbarini, N., Hördt, A., Christiansen, A.V., Foged, N.,

1024   Bjerg, P.L., and Auken, E.: Permeability estimation directly from logging-while-drilling

1025   induced   polarization   data, Water   Resources   Research, 54, 2851–2870,

1026   2018. https://doi.org/10.1002/2017WR022411.

1027 27. Fu, C., Di, Q., and An, Z.: Application of the CSAMT method to groundwater

1028   exploration in a metropolitan environment, Geophysics, 78 (5), B201–B209, 2013.

1029   https://doi.org/10.1190/geo2012-0533.1.

1030 28. Fusheng, G., Haiyan, Y., Zengqian, H., Zhichun, W., Ziyu, L., Guocan, W., Linfu, X., Ye,

1031   G., and Wanpeng, Z.: Structural setting of the Zoujiashan-Julong'an region, Xiangshan

1032   volcanic basin, China, interpreted from modern CSAMT data, Ore Geology Reviews, 150,

1033   105180, 2022. https://doi.org/10.1016/j.oregeorev.2022.105180.

1034 29. Gerke, H.H., Dusek, J., and Vogel, T.: Mass transfer effects in 2-D dual-permeability

1035   modeling of field preferential bromide leaching with drain effluent, Hydrol. Earth Syst.

1036   Sci. Discuss., 8, 5917–5967, 2011. https://doi.org/10.5194/hessd-8-5917-2011.

1037 30. Gleeson, T., Moosdorf, N., Hartmann, J., and van Beek, L.P.H.: A glimpse beneath

1038   earth's surface: Global hydrogeology maps (GLHYMPS) of permeability and porosity,

Geophysical Research Letters, 41(11), 3891–3898, 2014. https://doi.org/10.1002/2014GL059856.

31. Glover, P.W.J.: Geophysical properties of the near surface Earth: electrical properties, Treatise on Geophysics, 11, 89–137, 2015. https://doi.org/10.1016/B978-0-444-53802-4.00189-5.

32. Glover, P.W.J.: What is the cementation exponent? A new interpretation, The Leading Edge, 28(1), 82–85, 2009. https://doi.org/10.1190/1.3064150.

33. Gonzalez-Duque, D., Gomez-Velez, J.D., Person, M.A., Kelley, S., Key, K., and Lucero, D.: Groundwater Circulation Within the Mountain Block: Combining Flow and Transport Models With Magnetotelluric Observations to Untangle Its Nested Nature, Water Resources Research, 60(4), e2023WR035906, 2024. https://doi.org/10.1029/2023WR035906.

34. Hasan, M., and Shang, Y.: Geophysical evaluation of geological model uncertainty for infrastructure design and groundwater assessments, Engineering Geology, 299, 106560, 2022. https://doi.org/10.1016/j.enggeo.2022.106560.

35. Hasan, M., Shang, Y., Jin, W., and Akhter, G.: Estimation of hydraulic parameters in a hard rock aquifer using integrated surface geoelectrical method and pumping test data in southeast Guangdong China, Geosci J, 25 (2), 223–242, 2021. https://doi.org/10.1007/s12303-020-0018-7.

36. Hasan, M., Su, L., Cui, P., and Shang, Y.: Development of deep-underground engineering structures via 2D and 3D RQD prediction using non-invasive CSAMT, Scientific Reports, 15, 1403, 2025. https://doi.org/10.1038/s41598-025-85626-7.

1061   37. Herckenrath, D., Auken, E., Christiansen, L., Behroozmand, A.A., and Bauer‑Gottwein,

1062   P.: Coupled hydrogeophysical inversion using time-lapse magnetic resonance sounding

1063   and time-lapse gravity data for hydraulic aquifer testing: Will it work in practice? Water

1064   Resources Research, 48(1), W01539, 2012. https://doi.org/10.1029/2011WR010411.

1065   38. Herckenrath, D., Odlum, N., Nenna, V., Knight, R., Auken, E., and Bauer‑Gottwein, P.:

1066   Calibrating a Salt Water Intrusion Model with Time-Domain Electromagnetic Data,

1067   Groundwater, 51(3), 385–397, 2013. https://doi.org/10.1111/j.1745-6584.2012.00974.x.

1068   39. Hinnell, A.C., Ferré, T.P.A., Vrugt, J.A., Huisman, J.A., Moysey, S., Rings, J., and

1069   Kowalsky, M.B.: Improved extraction of hydrologic information from geophysical data

1070   through coupled hydrogeophysical inversion, Water Resources Research, 46(4), W00D40,

1071   2010. https://doi.org/10.1029/2008WR007060.

1072   40. Hu, X.Y., Peng, R.H., Wu, G.J., Wang, W.P., Huo, G.P., and Han, B.: Mineral

1073   exploration using CSAMT data: application to Longmen region metallogenic belt,

1074   Guangdong Province, China, Geophysics, 78, B111–B119, 2013.

1075   https://doi.org/10.1190/geo2012-0115.1.

1076   41. Ingebritsen, S.E., and Manning, C.E.: Permeability of the continental crust: dynamic

1077   variations inferred from seismicity and metamorphism, Geofluids, 10, 193–205, 2010.

1078   https://doi.org/10.1111/j.1468-8123.2010.00278.x.

1079   42. ISRM.: Suggested methods for rock characterization, testing and monitoring: 2007–2014,

1080   Springer, 2015. https://doi.org/10.1007/978-3-319-07713-0.

1081   43. Jardani, A., Revil, A., Santos, F., Fauchard, C., and Dupont, J.P.: Detection of

1082   preferential infiltration pathways in sinkholes using joint inversion of self‑potential and

1083 EM‑34 conductivity data, Geophysical Prospecting, 55(5), 749–760, 2007.

1084 https://doi.org/10.1111/j.1365-2478.2007.00638.x.

1085 44. Jasechko, S., Seybold, H., Perrone, D., Fan, Y., Shamsudduha, M., Taylor, R.G., Fallatah,

1086 O., and Kirchner, J.W.: Rapid groundwater decline and some cases of recovery in

1087 aquifers globally, Nature, 625, 715–721, 2024. https://doi.org/10.1038/s41586-023-

1088 06879-8.

1089 45. Jiang, X.W., Wan, L., Wang, J.Z., Yin, B.X., Fu, W.X., and Lin, C.H.: Field

1090 identification of groundwater flow systems and hydraulic traps in drainage basins using a

1091 geophysical method, Geophysical Research Letters, 41(8), 2812–2819, 2014.

1092 https://doi.org/10.1002/2014GL059579.

1093 46. Kouadio, K.L., Liu, R., Malory, A.O., and Liu, C.: A novel approach for water reservoir

1094 mapping using controlled source audio-frequency magnetotelluric in Xingning area,

1095 Hunan Province, China, Geophysical Prospecting, 71, 1708–1727, 2023.

1096 https://doi.org/10.1111/1365-2478.13385.

1097 47. Laghari, A.N., Vanham, D., and Rauch, W.: The Indus basin in the framework of current

1098 and future water resources management, Hydrology and Earth System Sciences, 16 (4),

1099 1063–1083, 2012. https://doi.org/10.5194/hess-16-1063-2012.

1100 48. Majumdar, R.K., and Das, D.: Hydrological characterization and estimation of aquifer

1101 properties from electrical sounding data in Sagar Island region, South 24 Parganas, West

1102 Bengal, India, Asian J Earth Sci, 4, 60–74, 2011.

1103 http://dx.doi.org/10.3923/ajes.2011.60.74.

1104   49. Manning, C.E., and Ingebritsen, S.E.: Permeability of the continental crust: Implications

1105   of geothermal data and metamorphic systems, Reviews of Geophysics, 37(1), 127–150,

1106   1999. https://doi.org/10.1029/1998RG900002.

1107   50. Mira Geoscience Ltd.: GOCAD Mining Suite 3D Geological Modeling Software. Nancy

1108   University, Lorraine, France, 1999.

1109   51. Mudunuru, M.K., Cromwell, E.L.D., Wang, H., and Chen, X.: Deep learning to estimate

1110   permeability using geophysical data, Advances in Water Resources, 167, 104272, 2022.

1111   https://doi.org/10.1016/j.advwatres.2022.104272.

1112   52. Niwas, S., and De Lima, O.A.L.: Aquifer parameter estimation from surface resistivity

1113   data, Groundwater, 41, 94–99, 2003. https://doi.org/10.1111/j.1745-6584.2003.tb02572.x.

1114   53. Nwosu, L.I., Nwankwo, C.N., and Ekine, A.S.: Geoelectric investigation of the hydraulic

1115   properties of the aquiferous zones for evaluation of groundwater potentials in the

1116   complex geological area of imostate, Nigeria, Asian J Earth Sci, 6, 1–15, 2013.

1117   https://scialert.net/abstract/?doi=ajes.2013.1.15.

1118   54. Pellet, H., Arfib, B., Henry, P., Touron, S., and Gassier, G.: Mesoscale permeability

1119   variations estimated from natural airflows in the decorated Cosquer Cave (southeastern

1120   France), Hydrol. Earth Syst. Sci., 28, 4035–4057, 2024. https://doi.org/10.5194/hess-28-

1121   4035-2024.

1122   55. Phoenix Geophysics CMTPro, The Canadian Phoenix CMT Pro Version software for

1123   CSAMT data processing. Toronto, Ontario, Canada, 2020.

1124   56. Phoenix Geophysics CSAMT-SW, The Canadian Phoenix CSAMT-SW Version software

1125   for CSAMT data inversion. Toronto, Ontario, Canada, 2020.

1126 57. Pollock, D., and Cirpka, O.A.: Fully coupled hydrogeophysical inversion of a laboratory
1127   salt tracer experiment monitored by electrical resistivity tomography, Water Resources
1128   Research, 48(1), W01505, 2012. https://doi.org/10.1029/2011WR010779.

1129 58. Qin, X.: Application of Unwedge program to geological stability analysis of deep buried
1130   deposits, Comprehensive, 8, 270–273, 2017 (In Chinese).

1131 59. Revil, A., and Cathles III, L.M.: Permeability of shaly sands, Water Resources Research,
1132   35(3), 651–662, 1999. https://doi.org/10.1029/98WR02700.

1133 60. Rodi, W., and Mackie, R.L.: Nonlinear conjugate gradients algorithm for 2-D
1134   magnetotelluric   inversion, Geophysics, 66   (1),   174–187,   2001.
1135   https://doi.org/10.1190/1.1444893.

1136 61. Saar, M.O., and Manga, M.: Depth dependence of permeability in the Oregon Cascades
1137   inferred from hydrogeologic, thermal, seismic, and magmatic modeling constraints,
1138   Journal   of   Geophysical   Research,   109(B4),   B04204,   2004.
1139   https://doi.org/10.1029/2003JB002855

1140 62. Simpson, F., and Bahr, K.: Practical magnetotellurics. Cambridge University Press,
1141   Cambridge. 254 pp, 2005. https://doi.org/10.1017/CBO9780511614095.

1142 63. Singh, K.P.: Nonlinear estimation of aquifer parameters from surficial resistivity
1143   measurements, Hydrology and Earth System Sciences Discussions, 2 (3), 917–938, 2005.
1144   https://doi.org/10.5194/hessd-2-917-2005.

1145 64. Smith, J.T., and Booker, J.R.: Rapid inversion of two-and three-dimensional
1146   magnetotelluric data, Journal of Geophysical Research: Solid Earth, 96 (B3), 3905–3922,
1147   1991. https://doi.org/10.1029/90JB02416.

1148 65. Soupios, P.M., Kouli, M., Vallianatos, F., Vafidis, A., and Stavroulakis, G.: Estimation of

1149   aquifer hydraulic parameters from surficial geophysical methods: a case study of Keritis

1150   Basin   in   Chania   (Crete–Greece),   J   Hydrol,   1,   122–131,   2007.

1151   https://doi.org/10.1016/j.jhydrol.2007.02.028.

1152 66. Wada, Y., Van Beek, L.P., Van Kempen, C.M., Reckman, J.W., Vasak, S., and Bierkens,

1153   M.F.: Global depletion of groundwater resources, Geophysical Research Letters, 37 (20),

1154   L20402, 2010. https://doi.org/10.1029/2010GL044571.

1155 67. Wang, R., Yin, C., Wang, M., and Di, Q.: Laterally constrained inversion for CSAMT

1156   data   interpretation,   Journal   of   Applied   Geophysics,   121,   63–70,   2015.

1157   https://doi.org/10.1016/j.jappgeo.2015.07.009.

1158 68. Waxman, M.H., and Smits, L.J.M.: Electrical conductivities in oil-bearing shaly sands,

1159   Society   of   Petroleum   Engineers   Journal,   8(02),   107–122,   1968.

1160   https://doi.org/10.2118/1863-A.

1161 69. Webring, M.W.: MINC: A Gridding Program Based on Minimum Curvature: U.S.

1162   Geological   Survey   Open   File   Report,   81–1224,   p.   41p,   1981.

1163   https://doi.org/10.3133/ofr811224.

1164 70. Worthington, S.R.H., Davies, G.J., and Alexander, E.C. Jr.: Enhancement of bedrock

1165   permeability   by   weathering,   Earth-Sci   Rev,   160,   188–202,   2016.

1166   https://doi.org/10.1016/j.earscirev.2016.07.002.

1167 71. Yan, Y., Ma, L., Qian, J., Zhao, G., Fang, Y., Ma, H., and Wang, J.: Estimating

1168   permeability of rock fracture based on geometrical aperture using geoelectrical

1169   monitoring,   Journal   of   Hydrology,   644,   132067,   2024.

1170   https://doi.org/10.1016/j.jhydrol.2024.132067.

1171   72. Yang, J., Zhang, H., and Cui, Z.: Stability Analysis and Countermeasures of Rock Block

1172   in Underground Cavern, Guangdong Water Resources and Hydropower 5, 23–27, 2021

1173   (In Chinese)

1174   73. Zhang, M., Farquharson, C.G., and Liu, C.: Improved controlled source audio-frequency

1175   magnetotelluric method apparent resistivity pseudo-sections based on the frequency and

1176   frequency–spatial gradients of electromagnetic fields, Geophysical Prospecting, 69, 474–

1177   490, 2021. https://doi.org/10.1111/1365-2478.13059.

1178   74. Zhu, L., Gong, H., Dai, Z., Guo, G., and Teatini, P.: Modeling 3-D permeability

1179   distribution in alluvial fans using facies architecture and geophysical acquisitions, Hydrol.

1180   Earth Syst. Sci., 21, 721–733, 2017. https://doi.org/10.5194/hess-21-721-2017.

1181   75. Zonge, K.L., and Hughes, L.J.: Kenneth L. Zonge and Larry J. Hughes, (1991), "9.

1182   Controlled Source Audio-Frequency Magnetotellurics," Investigations in Geophysics,

1183   713–810, 1991. https://doi.org/10.1190/1.9781560802686.ch9.